

Provided for non-commercial research and education use.
Not for reproduction, distribution or commercial use.



This article appeared in a journal published by Elsevier. The attached copy is furnished to the author for internal non-commercial research and education use, including for instruction at the authors institution and sharing with colleagues.

Other uses, including reproduction and distribution, or selling or licensing copies, or posting to personal, institutional or third party websites are prohibited.

In most cases authors are permitted to post their version of the article (e.g. in Word or Tex form) to their personal website or institutional repository. Authors requiring further information regarding Elsevier's archiving and manuscript policies are encouraged to visit:

<http://www.elsevier.com/authorsrights>



Contents lists available at SciVerse ScienceDirect

Journal of African Earth Sciences

journal homepage: www.elsevier.com/locate/jafrearsci

The Pan-African Kekem gabbro-norite (West-Cameroon), U–Pb zircon age, geochemistry and Sr–Nd isotopes: Geodynamical implication for the evolution of the Central African fold belt



Maurice Kwékam^{a,*}, Pascal Affaton^b, Olivier Bruguier^c, Jean-Paul Liégeois^d, Gerald Hartmann^e, Emmanuel Njôngfang^f

^a Département des Sciences de la Terre, Faculté des Sciences, Université de Dschang, B.P. 67, Dschang, Cameroon

^b CEREGE, Aix-Marseille Université, CNRS, B.P. 80, Europôle méditerranéen de l'Arbois, 13545 Aix-en-Provence cedex 04, France

^c Géosciences Montpellier UMR5243-CNRS, Université Montpellier 2, Place E. Bataillon CC060, 34095 Montpellier cedex 05, France

^d Isotope Geology, Royal Museum for Central Africa, B-3080 Tervuren, Belgium

^e Geowissenschaftliches Zentrum Göttingen, GZG, Abt. Geochemie, Universität Göttingen, Goldschmidtstraße 1, 37077 Göttingen, Germany

^f Laboratoire de Géologie, Ecole Normale Supérieure, Université de Yaoundé I, B.P. 47, Yaoundé, Cameroon

ARTICLE INFO

Article history:

Received 11 August 2010

Received in revised form 2 February 2013

Accepted 26 March 2013

Available online 11 April 2013

Keywords:

Shoshonitic gabbro-norite

Garnet-spinel peridotite

Subduction-related fluid metasomatism

Late post-collision period

West-Cameroon

ABSTRACT

The Kekem shoshonitic gabbro-norite association is part of the high-K calc-alkaline (HKCA) post-collisional magmatism, a major feature of the Pan-African Belt in Cameroon. LA-ICP-MS U–Pb zircon analyses provide an age of 576 ± 4 Ma for the Kekem complex. This age is interpreted as dating the emplacement of the massif during the waning stage of the Pan-African orogeny. The latter is related to dextral movements along the Central Cameroon Shear Zone (CCSZ).

The REE patterns display enriched LREE ($La_N/Yb_N = 14.2\text{--}23.5$) while HREE present a nearly flat profile ($Dy_N/Yb_N = 1.3\text{--}1.7$), and the La/Sm and Sm/Yb ratios led to propose that the Kekem gabbro-norites have been derived from the partial melting of a garnet-spinel lherzolite mantle source. The negative Nb–Ta and Ti anomalies and the positive Pb anomalies indicate that this mantle source was modified by contribution of a subduction-related material. The low Ce/Pb (2.6–10.4) and Th/Yb ratios associated to high Ba/La ratios, indicate that source enrichment could be related to slab derived fluids. As a whole, the Kekem geochemical features suggest that primary gabbro-noritic magmas derived from a subduction-modified mantle source (metasomatised lithospheric mantle). Moderately high $^{86}Sr/^{87}Sr$ initial ratios (0.7068–0.7082), low ϵ_{Nd} (–5 to –9) and old Nd T_{DM} model ages (1.6–1.8 Ga) are interpreted to result from contamination of Neoproterozoic mantle by the Paleoproterozoic crust.

The ca. 576 Ma movements along the CCSZ are related to a Neoproterozoic metacratonization of the northern margin of the Congo craton during the Pan-African orogeny. This metacratonization led to vertical planar lithospheric delamination along lithospheric transcurrent faults, asthenospheric uprise and partial melting of the Paleoproterozoic lithospheric mantle.

© 2013 Elsevier Ltd. All rights reserved.

1. Introduction

The Kekem gabbro-norite is a small mafic pluton in West-Cameroon. It results from the high-K calc-alkaline post-collisional magmatic activities along of Centre Cameroon Shear Zone (CCSZ). This magmatism, dated at 630–540 Ma (Toteu et al., 2004, and references therein) is a major feature of the central domain of the Pan-African fold belt in Cameroon. Key issues relate to the amount of remobilised crust in the source of the magmas, the age diversity

and also their actual location in the Central African mobile belt (Fig. 1a). This belt is considered as resulting from the convergence of the Congo and West-African cratons with the Saharan metacraton during the amalgamation of the Gondwana supercontinent (Abdelsalam et al., 2002).

On the northern margin of the Congo craton in West Cameroon, the post-collisional Pan-African gabbro-norite intrusion of Kekem is the only known mafic pluton. Country-rocks are gneisses and migmatitic granites. This gabbro-norite intrusion has been previously interpreted as the product of subduction-related arc magmatism (Kwékam, 2005; Kwékam et al., 2007). However, proposed geodynamical models for most Cameroonian magmatic rocks fit all a collisional setting within the former active margin (Ngako, 1999; Ngako et al., 2008; Toteu et al., 2006) or a post-collisional

* Corresponding author. Tel.: +237 77516684.

E-mail addresses: mkwekam@yahoo.fr (M. Kwékam), bruguier@gm.univ-montp2.fr (O. Bruguier), jean-paul.liegeois@africamuseum.be (J.-P. Liégeois), ghartma@gwdg.de (G. Hartmann).

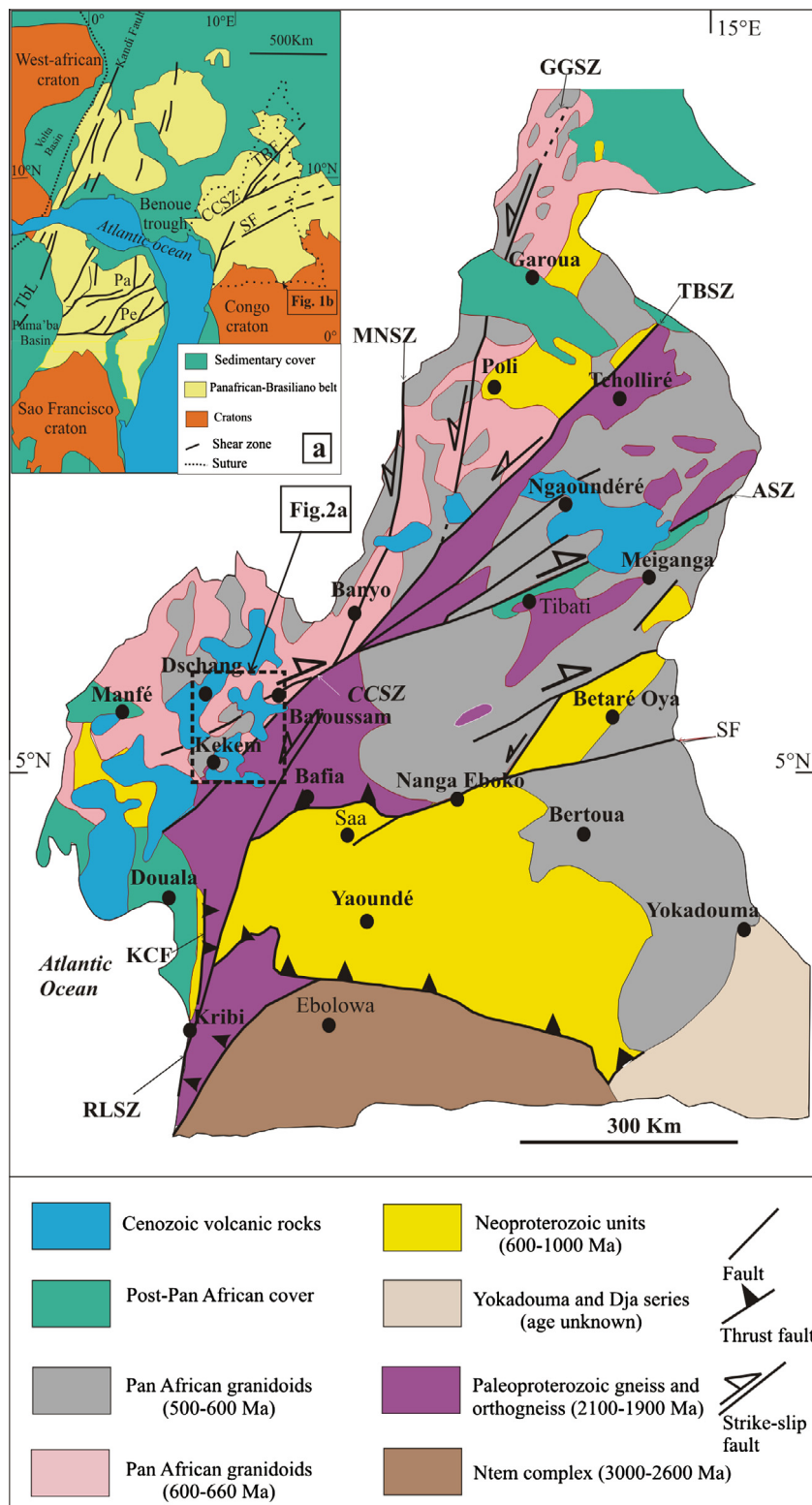


Fig. 1. (a) Geological sketch map of west-central Africa and northern Brazil with cratonic masses and the Pan-African-Brasiliano provinces of the Pan-Gondwana belt in a Pangea reconstruction; modified from Castaing et al. (1994) and Abdelsalam et al. (2002). TBF: Tcholliré-Banyo fault, CCSZ: Central Cameroon shear zone, SF: Sanaga fault, ASZ: Adamoua shear zone, Pa: Patos shear zone, Pe: Pernambuco shear zone. Dashed outline roughly marks the political boundary of Cameroon, (b) geological sketch map of Cameroon showing from the major lithotectonic domains (After Toteu et al., 2001; Ngako et al., 2008). GGSZ: Godé-Gormaya shear zone, MNZ: Mayo Nolti shear zone, RISZ: Rocher du Loup shear zone.

setting within the former passive margin (metacratonization of the northern boundary of the Congo craton; Kwékam et al., 2010). In this paper, zircon U–Pb dating, whole-rock major and trace ele-

ments geochemistry, and Rb–Sr and Sm–Nd isotopic data have been performed to determine more tightly the petrogenesis and geodynamical setting of this mafic pluton.

2. Geological setting

In Cameroon, the Precambrian complex is divided into two parts: (1) the Archaean (Ntem) – Palaeoproterozoic (Nyong) northern margin of the Congo craton and (2) the Neoproterozoic Central African fold belt (CAFB) including reworked older terranes. Toteu et al. (2004) divided the CAFB into three domains (Fig. 1b): (1) the southern or Yaoundé domain is made up of rocks deposited in a passive margin environment at the northern edge of the Congo craton; (2) the central or Adamawa-Yadé domain, located between the Sanaga Fault (SF) and the Tcholliré-Banyo Fault (TBF) It includes the study area which is composed of syn- to post-kinematic granitoids of mainly high-K calc-alkaline affinities; (3) the northern domain, also called western Cameroon domain, which consists of Neoproterozoic volcano-sedimentary schists and orthogneisses. Three main successive tectonic events, associated to the Pan-African collisional and post-collisional evolution, are defined in Cameroon: (1) crustal thickening (ca 630–610 Ma) marked by refolded thrust tectonics and widespread stretching lineation; (2) left lateral wrench movements (610–580 Ma), and (3) right lateral wrench movements, mainly presented in the Central Cameroon shear zone (CCSZ) and poorly dated at 585–540 Ma (Toteu et al., 2004; Ngako et al., 2008; Kwékam et al., 2010; Njanko et al., 2010). In Cameroon, the Pan-African belt was dextrally rotated during the third event. Recent works in the Adamawa-Yadé domain have also reported the occurrence of sinistral shear sense indicators associated to the same movement of direction as that revealed by the dextral shear markers (Ngako et al., 2003; Njonfang et al., 2006), suggesting a more complex kinematic evolution of the CCSZ (Ngako et al., 2008).

The Kekem gabbro-norite massif is part of numerous post-collisional plutons (Fig. 1b) which were emplaced within the central or Adamawa-Yadé domain of CAFB but norites are very rare in these plutons and their larger occurrence is in the Kekem pluton. In this area, these plutons, extending in age from 630 to 540 Ma, display

an evolving composition from calc-alkaline/S-type granitoids evolving to syn-tectonic calc-alkaline and S-type (630–610 Ma) to calc-alkaline to sub-alkaline granitoids (600–570 Ma) and finally to high-level alkaline towards 540 Ma in an extensional context (Toteu et al., 2004).

The small sub-ovoid Kekem massif (13 × 5.5 km²) is oriented N–S. It intruded a Palaeoproterozoic reworked basement on its northern and north-eastern edge (2.1 Ga banded garnet-sillimanite-pyroxene gneisses, Fig. 2a; Penaye et al., 2004), and an undated migmatitic granite to the south-east (Tagne-Kamga, 2003). It outcrops at the intersection of N–S and NE–SW regional faults and is overlain by Tertiary-Quaternary volcanic rocks of the Cameroon Line on its western edge (Fig. 2b).

To the north of Kekem, in the Dschang area, the gneiss shows N110 to N140°E foliation that is often wavy by NE–SW folding. These gneisses were later affected by mylonitic NE–SW (N50°E) dextral shear movements which are well evidenced at the south-eastern edge of the Fomopéa complex and by a N–S sinistral fault (Fig. 2a, Kwékam et al., 2010; Njanko et al., 2010). The contact between the gneissic country-rock and the Kekem massif can be observed at the northern enter of the Bayon village, where some blocks of norite display a slight mineral preferential orientation. A NNE–SSW flow structure is observed in the migmatitic granite. To the south of the Bayon village, this migmatitic granite is cross-cut by the Kekem massif, which in turn is locally crosscut by pegmatitic dykes, as a consequence of an intense hydrothermal activity.

3. Petrography

The Kekem gabbro-norites outcrop only as heterogeneous blocks in a coffee plantation and their observation is uneasy. Mapping of the two facies cannot be setup, however, following Kwékam (2005), the norites are be considered predominant and the gabbros mainly located at the border of the massif.

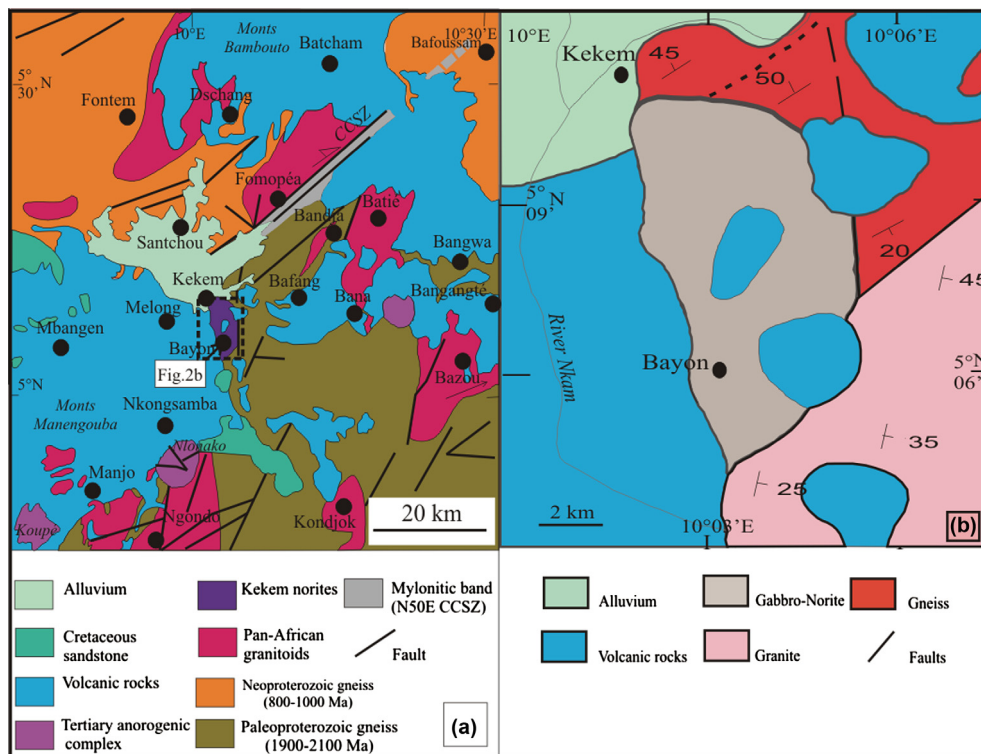


Fig. 2. (a) Extract of West-Cameroon geological map from Dumort (1968) showing the locality of the Kekem plutonic and its neighbouring plutons and (b) Kekem norites geological map.

The gabbros, mostly fine to medium-grained, are composed of clinopyroxene (diopside), phlogopite, plagioclase and oxides. Diopside crystals (6–10%) are euhedral and often surrounded by hornblende (actinote). Phlogopite (5–10%) is interstitial and partially surrounds pyroxenes; large flakes of phlogopite are poikilitic and sometimes display flexural deformation. They enclose zircon, plagioclase and pyroxene crystals. Plagioclase (30–55%) displays clusters of stubby crystals forming the framework of the rock. Some idiomorphic crystals of plagioclase show normal zoning (Fig. 3e–f). The plagioclase phenocrysts are sometimes broken (Fig. 3d). Accessory minerals include ilmenite, magnetite, apatite and zircon.

The norites, mostly medium-grained, are mainly made up of plagioclase (40–50%), orthopyroxene (enstatite, 20–30%), clinopyroxene (diopside, 20%), phlogopite (10–20%), and K-feldspar (<5%); accessory minerals are ilmenite, Cr-rich magnetite, rutile, apatite and zircon. Rare facies (e.g. sample Nk6) are rich in orthopyroxene (40%) with usually lamellar structure (Fig. 3h). Sample NK6 displays a particular cumulus microtexture in which plagioclase develops large crystals enclosing many small crystals. Orthopyroxene crystals and needles of an unknown coloured mineral occur in plagioclase crystals; comparable Fe–Ti oxide needles can be observed in places (Fig. 3a). Inclusions in pyroxene are mainly Cr-rich magnetite and rutile needles. Albite appears as exsolved globular in plagioclase (Fig. 3a). This exsolution resulted in the formation of secondary albite in the host plagioclase. Some orthopyroxene sections display titanomagnetite needles. Magmatic reaction texture is often observed within plagioclase – orthopyroxene – phlogopite association, such as a symplectite intergrowth of orthopyroxene and phlogopite. Secondary oxides after phlogopite and pyroxene are developed in some samples, and greenish phlogopite is replaced by chlorite.

In gabbro, clinopyroxene (augite particularly) seems crystallize before plagioclase and phlogopite. In Norite, clinopyroxene and plagioclase crystallized before orthopyroxene and phlogopite. Clinopyroxene–orthopyroxene twin lamellae suggest the later crystallization of orthopyroxene from clinopyroxene by exsolution and small orthopyroxene sections occur in plagioclase interstices in norites (Fig. 3f). These microtextures lead to suggest that norites are probably derived from gabbros by partial transformation of clinopyroxene to orthopyroxene. Large flakes of phlogopite develop irregular contour in norite NK6 suggesting disequilibrium during late P–T conditions (Fig. 3g).

4. Analytical techniques

4.1. Mineralogical analyses

Major element compositions of minerals were determined in thin sections by EPMA on a CAMECA SX-100 instrument equipped with five wavelength-dispersive X-ray spectrometers (WDS) at the Service Microsonde-Sud (Université Montpellier 2). The analyses were done with 20 kV accelerating voltage, a focused (3 μm) beam of 10 nA and counting times of 20–30 s. Concentrations are obtained from raw intensities using the “X-PHI” quantification procedure (Merlet, 1994). Natural minerals, synthetic oxides and pure metals are used as standards.

4.2. Laser ablation U–Th–Pb analyses

The sample selected for laser ablation U–Th–Pb geochronology was processed by crushing, heavy liquid and magnetic separation following conventional techniques (e.g. Bosch et al., 1996). Zircons from the non magnetic fractions were hand-picked and mounted along with chips of the G91500 zircon standard (Wiedenbeck et al., 1995) onto adhesive tape. The grains were then enclosed in

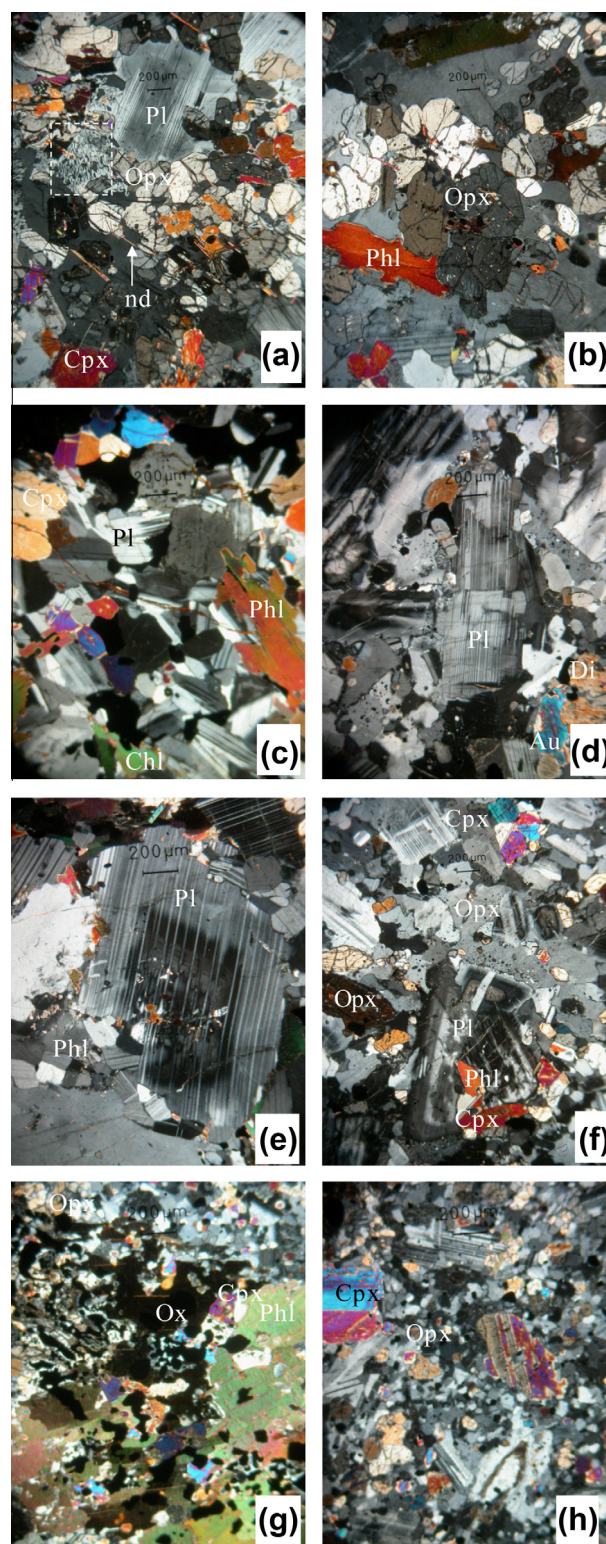


Fig. 3. Microscopic photos showing the micro texture: (a and b) NK6, Orthopyroxene-cumulated, in frame albite-exsolved, Cpx, clinopyroxene, Opx, orthopyroxene, Phl, phlogopite, Pl, plagioclase, Ox, oxide, nd, needle of rutile. This section have more abundance of orthopyroxene, (c–e) Gabbro (NK9, NK11, NK2), plagioclase is more abundant, phlogopite are rare, in NK2 (e), plagioclase displays normal zoning and contents inclusions of Cpx; in NK11 (d), large crystal of plagioclase is broken. (F–h) norites (NK1 and NK5), f section of NK1 showing zoning in plagioclase and interstitial pyroxene and phlogopite, g, unstable flake of phlogopite with abundant secondary oxide, h, exsolution lamellae clinopyroxene in NK1.

Table 1
LA-ICP-MS U–Th–Pb dating of zircons from sample NK13.

Sample NK13	Pb (ppm)	U (ppm)	Th (ppm)	Th/U	²⁰⁸ Pb/ ²⁰⁶ Pb	²⁰⁷ Pb/ ²⁰⁶ Pb	²⁰⁷ Pb/ ²³⁵ U	²⁰⁶ Pb/ ²³⁸ U	$\pm(1\sigma)$	Rho	Apparent ²⁰⁶ Pb/ ²³⁸ U	$\pm(1\sigma)$	Ages (Ma)	²⁰⁷ Pb/ ²⁰⁶ Pb	$\pm(1\sigma)$
pk1	15	133	161	1.22	0.360	0.05940	0.00013	0.73866	0.00579	0.96	557	4	582	5	5
pk2	13	115	129	1.12	0.334	0.05924	0.00014	0.74572	0.00649	0.96	563	5	576	5	5
pk3	14	125	150	1.19	0.334	0.05944	0.00049	0.75510	0.00950	0.76	568	5	583	18	18
pk4	14	126	140	1.11	0.341	0.05912	0.00013	0.74313	0.01199	0.99	562	9	571	5	5
pk5	16	146	169	1.15	0.346	0.05960	0.00040	0.75035	0.01007	0.87	563	6	589	14	14
pk6	14	130	162	1.24	0.367	0.05932	0.00017	0.73029	0.01585	0.99	551	11	579	6	6
pk7	32	294	346	1.18	0.349	0.05904	0.00034	0.73129	0.00680	0.78	555	4	568	13	13
pk8	14	132	143	1.09	0.326	0.05899	0.00034	0.73674	0.00567	0.66	559	3	567	13	13
pk9	20	178	214	1.20	0.352	0.05929	0.00012	0.74085	0.00648	0.97	559	5	578	4	4
pk10	17	160	176	1.10	0.311	0.05898	0.00032	0.74553	0.01334	0.95	565	9	567	12	12
pk11	23	203	251	1.23	0.356	0.05941	0.00023	0.74657	0.01690	0.98	562	12	582	9	9
pk12	12	110	95	0.87	0.298	0.05909	0.00039	0.74221	0.00592	0.57	562	2	570	14	14
pk13	20	175	209	1.19	0.345	0.05935	0.00016	0.74972	0.00318	0.76	565	2	580	6	6
pk14	12	107	125	1.17	0.341	0.05913	0.00045	0.74585	0.01294	0.90	564	8	572	17	17
pk15	44	396	483	1.22	0.331	0.05906	0.00018	0.75426	0.01754	0.99	571	13	569	7	7

epoxy resin and polished to expose internal structures. Laser ablation analyses were conducted using a Geolas platform housing a 193 nm CompEx 102 laser from LambdaPhysik, which was connected to an Element XR ICP-MS from ThermoFinnigan at Géosciences Montpellier (UMR5243-CNRS Montpellier, France). Details of the analytical procedure are described in Bruguier et al. (2009) and Bosch et al. (2011) and are only briefly summarized below. Data were acquired in the peak-jumping mode with the laser operating at an energy density of 12 J cm⁻² and a frequency of 3 Hz. The laser spot size was 26 μm. Measured isotopic ratios were monitored with reference to the G91500 zircon standard. Pb/Pb ratios in the unknown zircons were mass-bias corrected using a power law whose parameters were determined by repetitive analysis of the reference material measured during the whole analytical session. This mass bias factor was used to correct the ²⁰⁷Pb/²⁰⁶Pb ratios measured on the unknown zircons and its associated error was added in quadrature to the ²⁰⁷Pb/²⁰⁶Pb ratios measured on each unknowns following the procedure described in Horstwood et al. (2003). Inter-element fractionation for U and Pb is more sensitive to analytical conditions and the Pb/U ratios of each batch of five unknowns were calibrated against the bias factor calculated using four standards bracketing the five unknowns. The mean Pb/U ratio of the four measured standards was used to calculate the inter-element fractionation and its error was then added in quadrature to the individual error measured on each ²⁰⁶Pb/²³⁸U unknown. Reproducibility of the standard Pb/U ratio was 0.6% (RSD; n = 10) for the whole LA-ICP-MS session required to analyse the sample and, repeated measurements of the G91500 zircon standard gave an average value of 0.07529 ± 0.00017 corresponding to a mass bias of 0.54%. Accurate common lead correction is difficult to achieve, mainly because of the isobaric interference of ²⁰⁴Hg on ²⁰⁴Pb. The contribution of ²⁰⁴Hg on ²⁰⁴Pb was estimated by measuring the ²⁰²Hg and assuming a ²⁰⁴Hg/²⁰²Hg natural isotopic composition of 0.2298. This allows monitoring the common lead content of the analysed grain, but corrections often result in spurious ages. Analyses yielding ²⁰⁴Pb were thus rejected and Table 1 reports only analyses for which no ²⁰⁴Pb was detected. Quoted ratios correspond to measured ratios corrected from background and mass discrimination (+elemental fractionation for the ²⁰⁶Pb/²³⁸U ratios). All ages have been calculated using the U and Th decay constants recommended by Steiger and Jaeger (1977). Analytical data were plotted and ages calculated using the IsoplotEx program (Ludwig, 2000). Individual analyses in the data table 1 and in concordia plots are ±1σ errors and uncertainties in ages are quoted in the text at the 2σ level.

4.3. Whole – rock geochemical analyses

Major elements analyses and trace elements of whole-rock samples were performed by inductively coupled plasma-mass spectrometry (ICP-MS) and X-ray fluorescence (XRF) at the Geowissenschaftliches Zentrum of Göttingen Georg-August Universität, Abteilung Geochemie, Germany. Major elements and some trace elements (Sc, V, Cr, Co, Ni, Zn, Ga, Rb, Sr, Zr, and Ba) were determined by XRF analysis on glass pills prepared with a lithium tetraborate flux. The analytical precision (2σ) is less than 1% for major elements (except for Fe, Na: 2% and LOI: ~10%) and around 5% for trace elements. Additional trace elements were analysed by ICP-MS. The analytical errors estimated according to rock standards JB3 and JA2 are about 15–20% for Nb and Ta, and <10% for other trace elements.

4.4. Rb–Sr and Sm–Nd isotopic analyses

In the first step around 100 mg of the samples were digested by an acid mixture of HNO₃ and HF at a temperature of 180 °C. The

separation of Sr and REE was performed on columns filled with the cation exchange resin AG 50 W-X8 with 2.5 M HCl. Nd separation from the REE was performed on a column filled with Hexyl di-ethyl hydrogen phosphate (HDEHP) coated Teflon with 0.18 M HCl. The isotopes of Sr and Nd were measured with a Finnigan TRITON mass spectrometer at the Geowissenschaftliches Zentrum of Göttingen Georg-August Universität, Abteilung Geochemie. Measurements were performed in static and in peak-jumping multicollector mode for Sr and for Nd respectively. Sr analyses were corrected for mass fractionation by normalization to $^{88}\text{Sr}/^{86}\text{Sr} = 8.375209$, while the Nd analyses were normalized to $^{146}\text{Nd}/^{144}\text{Nd} = 0.7219$. Repeated measurements of the standard NBS987 gave on average a value of 0.710244, with a reproducibility of 0.000007 (2σ). The Nd standard La Jolla was determined with an average of 0.511845 ± 0.000005 . The blanks were negligible, ranging, for Sr from 100 to 200 pg and for Nd around 100 pg.

Four Sr and Nd compositions were also measured at Isotope Geology laboratory, Royal Museum of Central Africa, Tervuren (Belgium), on a VG Sector 54 TIMS. The external reproducibility on NBS987 standard solution was 0.710255 ± 0.000015 during the period of measurement. Sr compositions were corrected to a value of 0.710250 for NBS987 and fractionation corrected by reference to a $^{86}\text{Sr}/^{88}\text{Sr}$ value of 0.1194. The external reproducibility on La Jolla standard solution was 0.511837 ± 0.000015 . Nd compositions were corrected to a value of 0.511858 for La Jolla standard and fractionation corrected to $^{146}\text{Nd}/^{144}\text{Nd} = 0.7219$.

5. Results

5.1. Zircon U–Pb dating of the intrusion

Zircons were extracted from a gabbro sample (NK13) and consist of a uniform population of large ($>100 \mu\text{m}$) light brown grains, with euhedral shapes and sharp angle terminations. Under binocular examination, the zircon grains show no evidence of complex internal structures such as inclusions or inheritance. The morphological characteristics of the grains suggest a magmatic origin. All analyzed grains have U concentrations broadly ranging from 100 to 400 ppm, in the range of typical gabbroic rocks (c. 50–400 ppm after Schärer et al., 1986 and Pedersen and Dunning, 1997). Fifteen spot analyses were performed on fifteen grains or fragments (Table 1). All data points are concordant at the 2σ level (Fig. 4) but are slightly located to the right of the concordia. The mean of the 15 spots is discordant and the calculated age

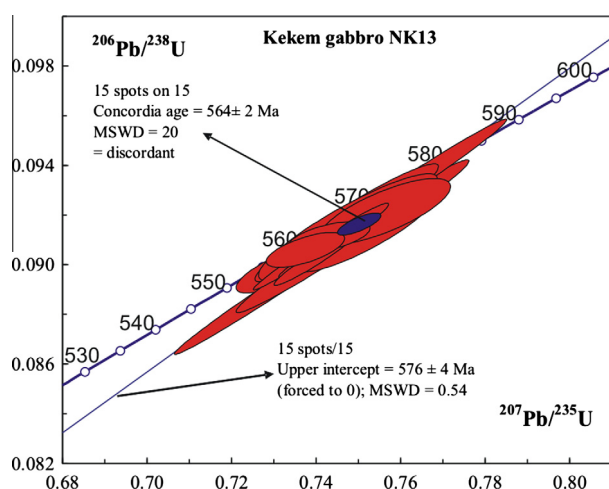


Fig. 4. U–Pb Concordia diagram for zircon analyses of the gabbro-norite NK13 of Kekem.

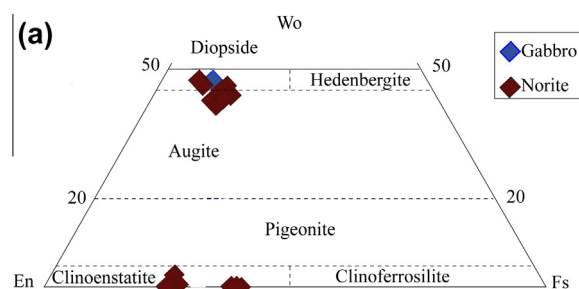


Fig. 5a. Classification of pyroxenes of the gabbro-norites from Kekem ($\text{Wo} = \text{Ca}/(\text{Fe}^{2+} + \text{Mn} + \text{Mg} + \text{Ca})$; $\text{En} = \text{Mg}/(\text{Fe}^{2+} + \text{Mn} + \text{Mg} + \text{Ca})$; $\text{Fs} = (\text{Fe}^{2+} + \text{Mn})/(\text{Fe}^{2+} + \text{Mn} + \text{Mg} + \text{Ca})$ after Morimoto et al. (1988).

($564 \pm 2 \text{ Ma}$) is associated with a high MSWD of 20. A slight Pb loss is then likely and it is justified calculating a discordia forced to 0. This discordia, calculated on the 15 spots, gives an age of $576 \pm 4 \text{ Ma}$ (MSWD = 0.54; Fig. 4), corresponding to a $^{207}\text{Pb}/^{206}\text{Pb}$ weighted mean age. This value is taken as our best age estimate for emplacement and crystallization of the gabbro sample NK13.

This age ($576 \pm 4 \text{ Ma}$) indicates that the Kekem complex is a late Pan-African intrusion that emplaced during the last Pan-African tectonic phase characterized by right lateral wrench movements and till now poorly dated between 585 and 540 Ma (Toteu et al., 2004). This last phase occurred mainly along the CCSZ where is located the Kekem complex.

5.2. Mineralogy

The pyroxenes are mainly diopside in the gabbros, and diopside and enstatite in the norites (Fig. 5a). In the gabbros, the compositions of diopside vary from $\text{Wo}_{42}\text{En}_{44}\text{Fs}_{14}$ to $\text{Wo}_{48}\text{En}_{42}\text{Fs}_{10}$ with X_{Mg} ranging from 0.75 to 0.81 while in the norites it is slightly less magnesian: $\text{Wo}_{45-46}\text{En}_{38-39}\text{Fs}_{17-15}$ and $X_{\text{Mg}} = 0.72-0.76$ (Table 2). In sample NK6, diopside is more magnesian ($X_{\text{Mg}} = 0.83-0.84$ and $\text{Wo}_{47-48}\text{En}_{43-44}\text{Fs}_{8-9}$) and richer in Ti.

Orthopyroxene (enstatite) composition is close to $\text{Wo}_{0-3}\text{En}_{60-75}\text{Fs}_{25-39}$ with $X_{\text{Mg}} = 0.61-0.75$. In NK6, orthopyroxene is also more magnesian ($X_{\text{Mg}} = 0.74-0.75$ and $\text{Wo}_{0-1}\text{En}_{72-75}\text{Fs}_{25-27}$). The mineralogical composition of sample NK6 is consistent with its chemical whole-rock composition (high MgO content). The orthopyroxene is generally poor in Al ($\text{Al}^{\text{IV}} = 0.0-0.014 \text{ p.f.u.}$).

Phlogopite (Fig. 5b) is less magnesian in gabbros ($X_{\text{Mg}} = 0.63-0.69$) than in norites where X_{Mg} is equal to 0.67–0.69 (Table 3). In sample NK6, it is unsurprisingly more magnesian ($X_{\text{Mg}} = 0.71-0.84$). This NK6 Opx-cummulated rock includes Ti-rich phlogopite ($\text{Ti} = 0.67-0.73$) and Ti-poor phlogopite ($\text{Ti} = 0.27-0.60$). In the gabbro NK13 phlogopite is Ti-rich ($\text{Ti} = 0.60-0.68$).

Feldspars display a large variation of compositions (Fig. 5c). They consist of plagioclase and alkali feldspar. Plagioclase ranges from labradorite to oligoclase. In gabbros, plagioclase is specifically basic ($\text{An}_{37-69}\text{Ab}_{62-31}$) while oligoclase ($\text{An}_{32-55}\text{Ab}_{44-66}$) and alkali feldspar ($\text{Or}_{32-87}\text{Ab}_{12-13}\text{An}_{0,3-7}$) are common in norites (Table 4). The composition of feldspars in norite NK6 is again specific: $\text{An}_{21-29}\text{Ab}_{69-78}$ for plagioclase and $\text{Or}_{32-36}\text{Ab}_{60-14}\text{An}_{11-1}$ for alkali feldspar.

The pyroxene thermobarometer of Putirka (2008) using equations 32c and 32d, allowed us to estimate the crystallization conditions of the different samples. In gabbro diopside displays low pressure (2.0–2.9 kbar) and temperatures around $1146.0-1174.5 \text{ }^\circ\text{C}$ with $K_{\text{D}}(\text{Fe-Mg})^{\text{Cpx-Liq}}$ between 0.26 and 0.29. In norite sample NK1 diopside occurs from 1141.8 to 1169.4 $^\circ\text{C}$ and 4.6 to 6.8 kbar with $K_{\text{D}}(\text{Fe-Mg})^{\text{Cpx-Liq}} = (0.269-0.275)$, and orthopyroxene displays $1120 \text{ }^\circ\text{C}$ and 4–5 kbar (Equations 29b and 28b after Put-

Table 2
Selected microprobe analyses of pyroxene.

Echantillon	Gabbros												Norites																		
	NK10 Di 94	NK13 Di 93	NK11 Di 27	NK11 Di 9	NK11 Di 12	NK11 Di 14	NK11 Di 24	NK11 Di 14	NK11 Di 23	NK6 Di 25	NK6 Di 21	NK6 Di 19	NK6 Di 19	NK6 Di 3	NK6 Di 3	NK6 Di 8	NK6 Di 5	NK6 Di 5	NK6 Di 6	NK6 Di 11	NK6 Di 18	NK6 Di 23	NK6 Di 14	NK1 En 2	NK1 En 4	NK1 En 32	NK1 En 32				
SiO ₂	52.850	53.365	51.429	51.984	52.532	51.718	51.708	51.718	51.718	51.718	51.718	51.718	51.718	51.718	51.718	51.718	51.718	51.718	51.718	51.718	51.718	51.718	51.718	51.718	51.718	51.718	51.718	51.718	51.718		
TiO ₂	0.505	0.007	0.441	0.328	0.455	0.386	0.470	0.490	0.466	0.288	0.643	0.288	0.288	0.288	0.288	0.288	0.288	0.288	0.288	0.288	0.288	0.288	0.288	0.288	0.288	0.288	0.288	0.288	0.288		
Al ₂ O ₃	1.638	0.592	1.870	1.741	2.140	1.850	2.192	2.396	2.167	1.554	2.527	2.634	2.549	1.432	1.885	1.548	1.885	2.066	0.481	0.511	1.069	0.659	0.575	0.516	0.756	0.669	0.670	0.732	0.732		
FeO _T	8.520	5.986	8.957	8.394	8.240	8.563	8.731	8.504	7.976	6.355	6.283	6.333	6.289	9.083	10.186	9.714	16.418	15.892	15.564	16.141	16.306	16.533	16.204	15.486	23.184	23.472	23.184	23.184	23.184		
Cr ₂ O ₃	0.000	0.000	0.000	0.000	0.000	0.000	0.000	0.000	0.000	0.000	0.000	0.000	0.000	0.000	0.000	0.000	0.000	0.000	0.000	0.000	0.000	0.000	0.000	0.000	0.000	0.000	0.000	0.000	0.000		
MnO	0.515	0.235	0.415	0.430	0.346	0.296	0.303	0.466	0.425	0.119	0.119	0.119	0.119	0.119	0.119	0.119	0.119	0.119	0.119	0.119	0.119	0.119	0.119	0.119	0.119	0.119	0.119	0.119	0.119		
MgO	14.440	14.755	14.445	13.838	13.708	13.685	13.529	13.476	13.425	14.161	14.161	14.161	14.154	13.449	13.361	13.226	12.921	12.921	12.921	12.921	12.921	12.921	12.921	12.921	12.921	12.921	12.921	12.921	12.921	12.921	
CaO	2.1860	23.24	20.409	21.958	21.375	21.897	21.742	22.060	22.149	22.899	22.824	22.899	22.824	21.520	20.877	21.668	20.877	20.877	20.877	20.877	20.877	20.877	20.877	20.877	20.877	20.877	20.877	20.877	20.877	20.877	
Na ₂ O	0.418	0.232	0.405	0.372	0.309	0.378	0.453	0.417	0.385	0.591	0.692	0.538	0.638	0.481	0.481	0.481	0.481	0.481	0.481	0.481	0.481	0.481	0.481	0.481	0.481	0.481	0.481	0.481	0.481	0.481	
K ₂ O	0.000	0.000	0.000	0.000	0.000	0.000	0.000	0.000	0.000	0.000	0.000	0.000	0.000	0.000	0.000	0.000	0.000	0.000	0.000	0.000	0.000	0.000	0.000	0.000	0.000	0.000	0.000	0.000	0.000	0.000	
Total	100.546	98.942	98.375	98.070	99.125	98.807	99.141	99.520	98.505	100.043	100.158	99.801	98.544	98.544	98.544	98.544	98.544	98.544	98.544	98.544	98.544	98.544	98.544	98.544	98.544	98.544	98.544	98.544	98.544	98.544	
Si	1.953	1.988	1.941	1.952	1.965	1.947	1.941	1.934	1.945	1.972	1.970	1.972	1.972	1.951	1.966	1.945	1.945	1.945	1.945	1.945	1.945	1.945	1.945	1.945	1.945	1.945	1.945	1.945	1.945	1.945	
Al IV	0.047	0.002	0.059	0.048	0.035	0.063	0.059	0.066	0.055	0.028	0.070	0.076	0.076	0.049	0.049	0.055	0.055	0.055	0.055	0.055	0.055	0.055	0.055	0.055	0.055	0.055	0.055	0.055	0.055	0.055	
Ti IV	0.000	0.000	0.000	0.000	0.000	0.000	0.000	0.000	0.000	0.000	0.000	0.000	0.000	0.000	0.000	0.000	0.000	0.000	0.000	0.000	0.000	0.000	0.000	0.000	0.000	0.000	0.000	0.000	0.000	0.000	
T	0.000	0.000	0.000	0.000	0.000	0.000	0.000	0.000	0.000	0.000	0.000	0.000	0.000	0.000	0.000	0.000	0.000	0.000	0.000	0.000	0.000	0.000	0.000	0.000	0.000	0.000	0.000	0.000	0.000	0.000	
Al VI	0.024	0.004	0.024	0.029	0.060	0.029	0.038	0.040	0.041	0.022	0.040	0.039	0.042	0.015	0.034	0.028	0.034	0.022	0.036	0.036	0.036	0.036	0.036	0.036	0.036	0.036	0.036	0.036	0.036	0.036	
Ti VI	0.014	0.000	0.013	0.009	0.013	0.011	0.013	0.014	0.013	0.008	0.018	0.018	0.016	0.008	0.009	0.012	0.012	0.012	0.012	0.012	0.012	0.012	0.012	0.012	0.012	0.012	0.012	0.012	0.012	0.012	0.012
Fe ³⁺	0.025	0.000	0.040	0.028	0.000	0.029	0.027	0.029	0.015	0.024	0.008	0.008	0.008	0.008	0.008	0.008	0.008	0.008	0.008	0.008	0.008	0.008	0.008	0.008	0.008	0.008	0.008	0.008	0.008	0.008	
Cr	0.000	0.001	0.000	0.000	0.000	0.000	0.000	0.000	0.000	0.000	0.000	0.000	0.000	0.000	0.000	0.000	0.000	0.000	0.000	0.000	0.000	0.000	0.000	0.000	0.000	0.000	0.000	0.000	0.000	0.000	
Fe ²⁺	0.142	0.181	0.212	0.218	0.234	0.222	0.227	0.220	0.222	0.154	0.153	0.141	0.139	0.219	0.249	0.255	0.238	0.242	0.252	0.252	0.248	0.251	0.253	0.253	0.246	0.373	0.379	0.373	0.373		
Mg	0.795	0.794	0.711	0.716	0.693	0.709	0.695	0.698	0.708	0.781	0.745	0.741	0.700	0.689	0.667	0.669	0.669	0.669	0.669	0.669	0.669	0.669	0.669	0.669	0.669	0.669	0.669	0.669	0.669	0.669	
Mn I	1.000	1.000	1.000	1.000	1.000	1.000	1.000	1.000	1.000	1.000	1.000	1.000	1.000	1.000	1.000	1.000	1.000	1.000	1.000	1.000	1.000	1.000	1.000	1.000	1.000	1.000	1.000	1.000	1.000	1.000	
Fe ³⁺	0.097	0.007	0.030	0.018	0.024	0.019	0.020	0.017	0.015	0.007	0.007	0.006	0.007	0.018	0.021	0.030	0.020	0.024	0.024	0.024	0.024	0.024	0.024	0.024	0.024	0.024	0.024	0.024	0.024	0.024	
Mn	0.016	0.007	0.013	0.014	0.011	0.009	0.010	0.015	0.014	0.004	0.004	0.004	0.004	0.012	0.011	0.011	0.010	0.009	0.009	0.009	0.009	0.009	0.009	0.009	0.009	0.009	0.009	0.009	0.009	0.009	
Ca	0.857	0.936	0.825	0.883	0.857	0.883	0.874	0.884	0.896	0.911	0.905	0.900	0.888	0.872	0.873	0.845	0.873	0.873	0.873	0.873	0.873	0.873	0.873	0.873	0.873	0.873	0.873	0.873	0.873	0.873	0.873
K	0.000	0.000	0.000	0.000	0.000	0.000	0.000	0.000	0.000	0.000	0.000	0.000	0.000	0.000	0.000	0.000	0.000	0.000	0.000	0.000	0.000	0.000	0.000	0.000	0.000	0.000	0.000	0.000	0.000	0.000	
Ni	0.000	0.000	0.000	0.000	0.000	0.000	0.000	0.000	0.000	0.000	0.000	0.000	0.000	0.000	0.000	0.000	0.000	0.000	0.000	0.000	0.000	0.000	0.000	0.000	0.000	0.000	0.000	0.000	0.000	0.000	
M2	1.000	0.987	1.000	1.000	1.000	1.000	1.000	1.000	1.000	1.000	1.000	1.000	1.000	1.000	1.000	1.000	1.000	1.000	1.000	1.000	1.000	1.000	1.000	1.000	1.000	1.000	1.000	1.000	1.000	1.000	
Mg/Fe-Mg	0.75	0.81	0.74	0.75	0.75	0.74	0.74	0.74	0.75	0.82	0.80	0.80	0.80	0.72	0.72	0.70	0.70	0.74	0.74	0.74	0.74	0.74	0.74	0.74	0.74	0.74	0.74	0.74	0.74	0.74	
Mg (En)	41.16	42.14	42.02	40.45	40.22	39.53	39.53	39.21	39.41	42.58	41.33	41.48	41.77	39.16	38.97	38.70	37.85	37.85	37.85	37.85	37.85	37.85	37.85	37.85	37.85	37.85	37.85	37.85	37.85	37.85	
Fe-Min (Fs)	14.46	9.97	15.30	14.33	14.22	14.45	14.81	14.65	13.85	9.85	10.62	10.49	10.74	15.80	15.43	17.39	15.98	15.98	15.98	15.98	15.98	15.98	15.98	15.98	15.98	15.98	15.98	15.98	15.98	15.98	
Ca (Wo)	44.38	47.88	42.67	45.65	45.33	45.76	45.66	46.14	46.74	47.57	48.04	48.04	47.50	45.04	45.60	43.91	45.62	45.62	45.62	45.62	45.62	45.62	45.62	45.62	45.62	45.62	45.62	45.62	45.62	45.62	45.62
Total	100.00	100.00	100.00	100.00	100.00	100.00	100.00	100.00	100.00	100.00	100.00	100.00	100.00	100.00	100.00	100.00	100.00	100.00	100.00	100.00	100.00	100.00	100.00	100.00	100.00	100.00	100.00	100.00	100.00	100.00	
Q	1.89	1.95	1.88	1.89	1.88	1.89	1.88	1.87	1.89	1.84	1.82	1.81	1.87	1.89	1.8																

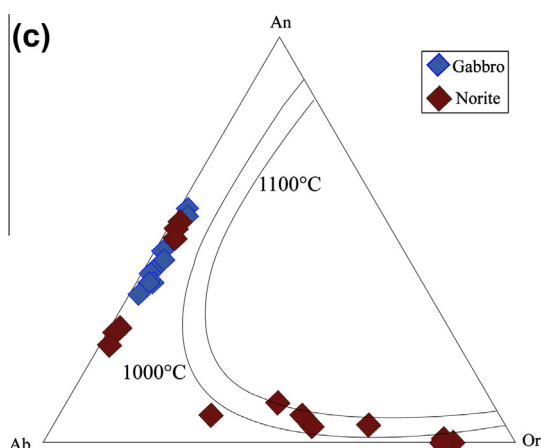


Fig. 5c. Classification of feldspars of the gabbro-norites from Kekem, with thermometry from Fuhrman and Lindsley (1998).

scatter but some rough correlations can be observed (Fig. 7a). SiO₂ and Al₂O₃ increase, CaO and Fe₂O₃ (total iron) decrease, with decreasing MgO. TiO₂ increases in gabbros, and exhibit scattered trend in norites, indicating relatively constant abundances. K₂O + Na₂O also increase with decreasing MgO.

Major element contents show that norites and gabbros do not belong to the same line of descent: for a given MgO content, gabbros are rich in Fe₂O₃, TiO₂, CaO, P₂O₅, Al₂O₃, Na₂O and poorer in SiO₂ and K₂O. This suggests different parental magmas or different evolution processes, that of the norites being more evolved and especially more potassic although norites have similar Mg# (atomic ratios, 49–61, except NK6, see below) than the gabbros (42–59). The norite sample NK6 has a high MgO content (nearly 14%) and Mg# (77), pointing to a cumulate character. Its high K₂O content confirms its linkage with the norite trend. Sample NK13 with a high MgO content (8.66%) but not cumulative in character, has the composition which is the closest to the primitive magma. Let us note that it is already enriched in K₂O (2.33%).

CIPW norms show that the gabbroic rocks are silica-saturated (no quartz and no significant nepheline), with high to moderate olivine (8.5–21.5 vol.%), ilmenite, magnetite and apatite contents; and relatively low diopside (3.2–4.4 vol.%), except NK13 (16.8 vol.%), which is moreover rich in hypersthene (11.3–17.0 vol.%). By contrast, norites are silica-saturated/oversaturated rocks (GK0 and NK3). They are normally enriched in alkali-feldspars and hypersthene. The cumulate NK6 is rich in hypersthene (33.4 vol.%), in agreement with its cumulate character.

5.3.2. Trace elements

Trace elements that are compatible in clinopyroxene, such as Sc, V and Co, decrease rapidly with MgO (Fig. 7b). Some transitional elements (Ni, Co, Cr) are more abundant in norites than in gabbros. Here also, two distinct lines of descent can be depicted for gabbros and norites, gabbros being generally depleted relatively to norites. Rb, Sr, Ba, elements incorporated by feldspars, do not display clear trends and are all very abundant: Sr: 680–1300 ppm in norites, 1250–1500 ppm in gabbros, Ba: 1200–2300 ppm in norites, 1400–3100 ppm in gabbros, Rb: 83–160 ppm in norites, 45–80 ppm in gabbros. This indicates a limited role of feldspars in the differentiation, in agreement with the common high Al₂O₃ content.

REE patterns display either negative or positive europium anomalies (Eu/Eu_n = 0.8–1.5). The REE patterns are LREE enriched relative to HREE (La_N/Yb_N = 14.2–23.5) while HREE present a nearly flat profile either in gabbros (Dy_N/Yb_N = 1.7–1.8) or in norites (Dy_N/Yb_N = 1.3–1.6). Sample NK6 yields a negative Sr anomaly that may

Table 4 Selected microprobe analyses of feldspar.

	Gabbros										Norites																										
	NK10	NK11	NK12	NK13	NK14	NK15	NK16	NK17	NK18	NK6	NK10	NK11	NK12	NK13	NK14	NK15	NK16	NK17	NK18	NK6																	
SiO ₂	58.300	58.630	58.150	57.300	54.370	57.620	58.370	57.840	58.470	56.480	53.964	53.181	53.924	58.998	56.458	57.101	55.879	58.479	55.253	54.799	54.147	54.413	64.028	64.208	64.912	66.263	64.926	65.003	62.673	62.181	61.174	61.715	62.163	63.285	64.662	64.814	
Al ₂ O ₃	26.180	25.890	25.960	26.550	28.360	26.550	26.010	26.260	25.810	26.920	29.351	29.284	29.651	29.507	26.136	27.158	27.979	26.107	28.656	29.079	28.987	28.982	18.884	19.703	20.582	18.664	18.569	23.231	23.994	23.863	24.709	24.141	19.473	20.936	20.052	20.552	
TiO ₂	0.036	0.014	0.046	0.014	0.026	0.030	0.024	0.064	0.035	0.020	0.009	0.029	0.025	0.035	0.036	0.034	0.030	0.083	0.010	0.027	0.052	0.047	0.072	0.051	0.094	0.110	0.040	0.000	0.000	0.000	0.000	0.000	0.001	2.716	0.033	0.037	
Cr ₂ O ₃	0.015	0.000	0.010	0.025	0.000	0.032	0.000	0.015	0.000	0.000	0.009	0.014	0.009	0.001	0.002	0.005	0.006	0.007	0.000	0.000	0.000	0.000	0.000	0.000	0.000	0.015	0.015	0.000	0.018	0.000	0.000	0.000	0.000	0.000	0.000	0.000	0.000
FeO	0.135	0.108	0.089	0.159	0.133	0.152	0.098	0.195	0.114	0.076	0.170	0.155	0.180	0.224	0.103	0.137	0.097	0.101	0.115	0.170	0.184	0.180	0.034	0.033	0.029	0.083	0.048	0.040	0.230	0.129	0.525	0.170	0.129	0.031	0.080	0.051	
MnO	0.010	0.000	0.000	0.000	0.010	0.010	0.000	0.014	0.011	0.024	0.000	0.000	0.000	0.000	0.004	0.008	0.017	0.015	0.011	0.013	0.011	0.008	0.000	0.000	0.000	0.000	0.000	0.000	0.010	0.000	0.013	0.011	0.018	0.000	0.000	0.000	
MgO	0.010	0.000	0.000	0.000	0.010	0.010	0.000	0.015	0.000	0.000	0.009	0.000	0.000	0.000	0.004	0.022	0.042	0.002	0.000	0.000	0.000	0.000	0.000	0.000	0.000	0.000	0.000	0.019	0.104	0.000	0.291	0.000	0.000	0.000	0.000		
CaO	7.850	8.140	8.070	8.780	10.820	8.620	8.160	8.400	7.950	9.380	11.238	11.389	11.632	11.590	7.506	9.014	8.370	9.799	10.561	10.989	11.166	11.045	0.062	0.084	1.101	1.569	0.262	0.149	5.017	5.520	5.716	6.170	5.674	1.096	2.366	1.594	
Na ₂ O	6.980	7.080	6.960	7.000	5.330	6.850	7.120	6.710	6.880	6.320	4.956	4.869	4.727	4.811	6.960	6.111	6.652	5.616	6.446	5.279	4.921	5.126	1.468	1.458	5.003	7.243	1.833	1.602	8.358	8.086	8.309	8.454	3.401	5.309	4.833		
K ₂ O	0.253	0.264	0.337	0.347	0.202	0.178	0.196	0.252	0.283	0.212	0.189	0.174	0.198	0.156	0.260	0.302	0.259	0.338	0.279	0.209	0.179	0.187	0.186	14.854	10.432	5.911	14.927	15.165	0.129	0.115	0.232	0.216	0.153	12.112	8.120	8.992	
NiO	0.000	0.000	0.000	0.000	0.000	0.000	0.000	0.000	0.000	0.000	0.000	0.000	0.000	0.000	0.000	0.000	0.000	0.000	0.000	0.000	0.000	0.000	0.000	0.000	0.000	0.000	0.000	0.000	0.000	0.000	0.000	0.000	0.000	0.000	0.000		
BaO	0.054	0.046	0.000	0.071	0.064	0.016	0.000	0.028	0.043	0.000	0.000	0.000	0.000	0.004	0.004	0.000	0.000	0.000	0.000	0.000	0.000	0.000	0.000	0.000	0.000	0.000	0.000	0.000	0.000	0.000	0.000	0.000	0.000	0.000	0.000	0.000	
Total	98.81	100.18	99.57	99.57	99.52	100.06	99.56	99.79	99.45	99.90	99.37	99.61	100.26	100.02	100.02	99.32	99.15	98.78	99.66	100.26	100.55	99.66	99.99	99.35	101.28	101.79	100.72	100.58	99.79	100.03	99.93	101.32	100.74	102.13	101.70	100.38	
Al ₂ SiO ₅	0.000	0.000	0.000	0.000	0.000	0.000	0.000	0.000	0.000	0.000	0.000	0.000	0.000	0.000	0.000	0.000	0.000	0.000	0.000	0.000	0.000	0.000	0.000	0.000	0.000	0.000	0.000	0.000	0.000	0.000	0.000	0.000	0.000	0.000	0.000		
Al	1.363	1.364	1.376	1.407	1.524	1.403	1.371	1.390	1.367	1.434	1.564	1.569	1.587	1.568	1.371	1.448	1.414	1.486	1.379	1.518	1.539	1.548	1.542	1.033	1.030	1.067	1.058	1.008	1.004	1.214	1.232	1.253	1.279	1.254	1.035	1.099	
Ti	0.001	0.000	0.000	0.000	0.000	0.001	0.001	0.001	0.001	0.001	0.001	0.001	0.001	0.001	0.001	0.001	0.001	0.001	0.001	0.001	0.001	0.001	0.001	0.001	0.001	0.001	0.001	0.001	0.001	0.001	0.001	0.001	0.001	0.001	0.001	0.001	
Cr	0.001	0.000	0.000	0.000	0.000	0.001	0.001	0.001	0.001	0.001	0.001	0.001	0.001	0.001	0.001	0.001	0.001	0.001	0.001	0.001	0.001	0.001	0.001	0.001	0.001	0.001	0.001	0.001	0.001	0.001	0.001	0.001	0.001	0.001	0.001	0.001	
Fe	0.005	0.004	0.003	0.006	0.005	0.006	0.004	0.007	0.004	0.003	0.006	0.006	0.007	0.008	0.004	0.005	0.004	0.005	0.004	0.006	0.007	0.007	0.001	0.001	0.001	0.001	0.001	0.002	0.002	0.009	0.005	0.020	0.006	0.005	0.001	0.003	0.002
Mg	0.001	0.000	0.000	0.001	0.000	0.000	0.001	0.000	0.001	0.000	0.000	0.000	0.000	0.000	0.001	0.001	0.001	0.001	0.000	0.001	0.000	0.000	0.000	0.000	0.000	0.000	0.000	0.000	0.000	0.000	0.000	0.000	0.000	0.000	0.000	0.000	
Mn	0.001	0.000	0.000	0.000	0.000	0.000	0.000	0.000	0.000	0.000	0.000	0.000	0.000	0.000	0.000	0.000	0.000	0.000	0.000	0.000	0.000	0.000	0.000	0.000	0.000	0.000	0.000	0.000	0.000	0.000	0.000	0.000	0.000	0.000	0.000	0.000	
Ca	0.377	0.390	0.389	0.423	0.527	0.414	0.392	0.404	0.383	0.454	0.544	0.554	0.566	0.560	0.359	0.437	0.405	0.473	0.380	0.508	0.529	0.542	0.534	0.003	0.004	0.053	0.074	0.007	0.028	0.262	0.273	0.290	0.268	0.053	0.113	0.077	
Na	0.607	0.614	0.606	0.584	0.470	0.596	0.618	0.585	0.599	0.554	0.434	0.429	0.416	0.420	0.602	0.536	0.583	0.490	0.577	0.475	0.429	0.448	0.132	0.131	0.437	0.618	0.163	0.142	0.718	0.694	0.699	0.712	0.722	0.297	0.458	0.423	
K	0.015	0.015	0.019	0.020	0.012	0.010	0.011	0.016	0.012	0.011	0.010	0.011	0.009	0.010	0.015	0.017	0.021	0.016	0.012	0.012	0.012	0.011	0.011	0.000	0.000	0.000	0.000	0.000	0.000	0.000	0.000	0.000	0.000	0.000	0.000	0.000	
Ni	0.000	0.000	0.000	0.000	0.000	0.000	0.000	0.000	0.000	0.000	0.000	0.000	0.000	0.000	0.000	0.000	0.000	0.000	0.000	0.000	0.000	0.000	0.000	0.000	0.000	0.000	0.000	0.000	0.000	0.000	0.000	0.000	0.000	0.000	0.000	0.000	
Ba	0.004	0.001	0.000	0.001	0.001	0.000	0.000	0.001	0.001	0.000	0.000	0.000	0.000	0.000	0.000	0.000	0.000	0.000	0.000	0.000	0.000	0.000	0.000	0.000	0.000	0.000	0.000	0.000	0.000	0.000	0.000	0.000	0.000	0.000	0.000	0.000	
Total	5.004	5.010	5.010	5.021	5.008	5.016	5.013	5.004																													

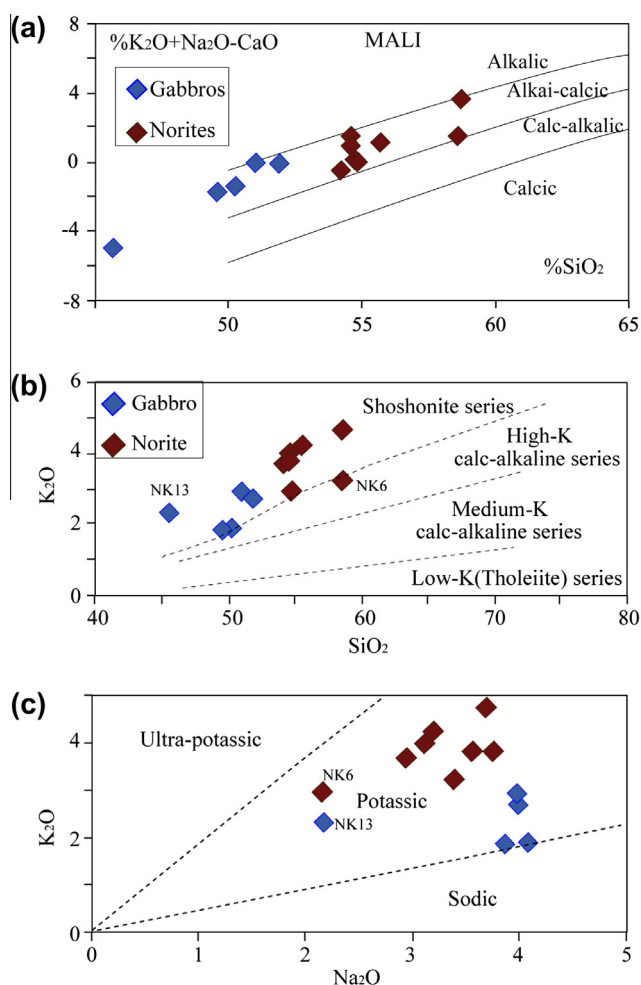


Fig. 6. (a) MALI diagram from Frost et al. (2001). Plot of $\text{Na}_2\text{O} + \text{K}_2\text{O} - \text{CaO}$ vs SiO_2 showing the alkali-calcic feature of the Kekem rocks, (b) K_2O vs SiO_2 diagram after Peccerillo and Taylor (1976), shows the shoshonitic affinity of gabbro-norites from Kekem and (c) K_2O vs Na_2O confirms the high-k feature of gabbro-norites from Kekem.

be related to plagioclase fractionation. Samples NK1 (Norite sample Fig. 8c) and NK9 (Gabbro sample Fig. 8a) have positive Eu and Sr anomalies, suggesting a slight accumulation of plagioclase. Strong Ta–Nb and Ti negative anomalies are observed while Ba is marking a positive anomaly (Fig. 8b–d), but Ti negative anomaly is less pronounced in gabbroic samples. On the contrary, Hf–Zr negative anomaly is more expressive in gabbro sample NK10 than in norites. The multi-element patterns of both groups are enriched in Sr, K, Rb, Ba, compared to MORB or to the lower crust although the gabbroic samples and some norite samples (NK1, NK3, NK8) are less enriched in K, Rb and Th (Fig. 8b–d). In Fig. 8e–f, the rocks of the Kekem pluton display a trend indicating that they belong to a same source, the least radiogenic sample NK6 being located close to the upper continental crust pole (Fig. 8f).

5.4. Rb–Sr and Sm–Nd isotope compositions

Nine whole-rock Sr and Nd isotope analyses were carried out and results are presented in Table 6. The Rb–Sr data define an errochron, with a very high MSWD of 223. The fact that the calculated age from this errochron (588 ± 120 Ma with a Sr initial ratio = 0.70734 ± 0.00071) encompasses the zircon age, suggests that the cause of the dispersion is either related to heterogeneous magma batches or to variable late magmatic interaction with the country-rocks. Individual $^{87}\text{Sr}/^{86}\text{Sr}$ Sr initial ratios calculated at 576 Ma

(U–Pb zircon age) vary from 0.7069 to 0.7082, with slightly higher values in gabbros (0.7075–0.7082) than in norites (0.7068–0.7071, with 0.7080 in NK6). Nd isotopes display negative ϵ_{Nd} ranging from –6 to –8.9 for the gabbros and from –5.2 to –7.6 for the norites with Nd TDM ranging from 1577 to 1889 Ma. The gabbros and the norites define two closed parallel trends, with NK6 norite within the gabbro trend (Fig. 9a). These trend and 1.6–1.9 Ga TDM model ages are indicative either of a mixing between a juvenile Neoproterozoic mantle source and a much older than 1.9 Ga lithospheric source (Archean) or of a mainly c. 2 Ga Paleoproterozoic with some limited Neoproterozoic asthenospheric mantle input bringing heat mantle input at the origin of the crustal melting. Considering that the Archean lithosphere is only known much to the South (Ntem Complex; Shang et al., 2007, 2010) and the slight extent of the trends, we privilege the latter solution.

6. Discussion

6.1. Fractional crystallization and crustal contamination

The low Cr and Ni contents of the Kekem rocks indicate a relatively evolved magma, consistent with their low MgO contents (except NK6 and NK13 samples). The samples show a range in MgO values that are coupled with significant variations in Sc, V, Cr, Co, suggesting the possible influence of fractional crystallization on their primitive magma composition. The normal zoning displayed by plagioclase crystals is an additional argument for fractional crystallization. Positive correlation between specific trace element concentrations and MgO suggests that the parental magma of the kekem gabbro-norite has undergone fractionation of magnesian clinopyroxene (Sc) \pm Cr-rich oxides (Cr and V). Decreases of MgO with CaO, Sc and V indicate that clinopyroxene fractionation has been important in both groups. Increases in Al_2O_3 and Sr with decreasing MgO indicate fractionation of a mineral assemblage without abundant plagioclase. The slightly negative Eu anomalies on the REE patterns and negative Sr anomalies on the primitive mantle-normalised patterns for sample NK6 could indicate early fractionation of plagioclase. In contrast, the positive Eu and Sr anomalies displayed by samples NK1 and NK9 indicate either cumulated plagioclase- or melt from cumulated material. The gabbros and norites exhibit different evolutionary trends, suggesting that they followed different paths of fractional crystallization or accumulation or/and post-magmatic alteration. Some fractionation of Fe–Ti oxides occurred in both groups. In general, gabbros and norites do not appear to be related by the fractionation process. Each group defines its own linear correlation trend that can be linked, on the one hand, to slight difference in their source (the most basic samples in each trend are different) and, on the other hand, to their crystallization history, including thermodynamic conditions, as mirrored by their distinct mineral compositions. The presence of clinopyroxene (Diopside) in gabbro and the lack of clinopyroxene-orthopyroxene equilibrium in norites suggest a thermodynamic change during the emplacement history of the massif. In fact, the progressive descent of MgO, FeO and CaO could reflect crystallization of Ti-oxide and diopside in gabbro with less magnesian phlogopite. Then following the precipitation of apatite and plagioclase mineral, the magma is depleted in CaO and Al_2O_3 , and at in a second step diopside, orthopyroxene and magnesian phlogopite crystallized. This observation is confirmed by more magnesian characteristic of norite ($\text{Mg}\# = 49\text{--}61$) than gabbro ($\text{Mg}\# = 44\text{--}59$). This enrichment in MgO for norite samples could indicate the contamination by gneissic country rocks. The more magnesian sample NK6 locates close to the upper crust in different diagrams (Figs. 8f and 10). The geodynamic context could also intervene,

Table 5
Major and trace elements analyses.

	Gabbros				Norites								
	NK13	NK10	NK 11	NK 2	NK9	NK 8	GK 0	NK 5	NK7	NK 1	NK 4	NK 3	NK 6
SiO ₂ (%)	45.67	49.60	50.30	51.00	51.90	54.20	58.60	54.70	55.70	54.60	54.60	58.70	54.80
TiO ₂	1.95	1.74	1.70	1.56	1.55	1.13	0.86	1.31	1.23	1.05	1.24	0.94	0.89
Al ₂ O ₃	12.88	18.00	19.00	18.90	19.00	14.90	15.60	15.80	15.40	17.60	17.20	16.70	10.00
Fe ₂ O ₃	13.11	11.10	9.88	9.24	8.83	8.67	6.56	8.12	7.80	7.79	8.25	6.11	9.15
MnO	0.17	0.19	0.16	0.17	0.16	0.14	0.10	0.13	0.12	0.13	0.13	0.10	0.14
MgO	8.66	4.01	3.77	3.33	3.20	5.84	4.62	4.61	4.61	3.81	3.74	2.60	13.75
CaO	9.48	7.50	7.42	6.98	6.83	7.05	5.15	6.98	6.34	6.50	6.07	4.71	5.18
Na ₂ O	2.17	3.86	4.08	3.98	3.99	2.95	3.39	3.11	3.18	3.56	3.74	3.68	2.15
K ₂ O	2.33	1.85	1.91	2.93	2.72	3.68	3.24	4.01	4.26	3.81	3.81	4.70	2.96
P ₂ O ₅	1.46	0.98	0.88	0.78	0.70	0.75	0.29	0.78	0.67	0.66	0.75	0.47	0.20
Total	97.87	98.82	99.10	98.87	98.89	99.30	98.40	99.54	99.31	99.51	99.53	98.71	99.21
K ₂ O + Na ₂ O	4.50	5.71	5.99	6.91	6.71	6.63	6.63	7.12	7.44	7.37	7.55	8.38	5.11
K ₂ O/Na ₂ O	1.07	0.48	0.47	0.74	0.68	1.25	0.96	1.29	1.34	1.07	1.02	1.28	1.38
<i>Norm</i>													
Quartz	0.0	0.0	0.0	0.0	0.0	0.0	7.3	0.0	0.8	0.0	0.0	4.6	0.0
Orthoclase	14.2	11.2	11.5	17.7	16.4	22.1	19.6	24.0	25.5	22.8	22.8	28.3	17.8
Albite	18.6	33.4	35.1	32.9	34.4	25.3	29.3	26.6	27.3	30.5	32.0	31.7	18.5
Anorthite	19.2	26.9	28.4	25.5	26.4	16.8	18.2	17.5	15.4	21.0	19.1	15.4	9.0
Nepheline	0.2	0.0	0.0	0.8	0.0	0.0	0.0	0.0	0.0	0.0	0.0	0.0	0.0
Diopside	16.8	4.4	3.2	4.3	3.3	11.7	5.1	10.6	10.2	6.3	5.7	4.6	12.7
Hypersthene	0.0	4.7	2.8	0.0	4.9	17.3	17.1	15.6	15.5	11.4	11.4	11.4	33.4
Olivine	21.5	12.0	12.0	12.5	8.5	1.5	0.0	0.0	0.0	3.2	3.4	0.0	4.8
Magnetite	2.3	2.0	1.7	1.6	1.6	1.5	1.2	1.4	1.4	1.4	1.4	1.1	1.6
Ilmenite	3.8	3.4	3.3	3.0	3.0	2.2	1.7	2.5	2.4	2.0	2.4	1.8	1.7
Corindon	0.0	0.0	0.0	0.0	0.0	0.0	0.0	0.0	0.0	0.0	0.0	0.0	0.0
Apatite	3.3	2.2	2.0	1.7	1.6	1.7	0.6	1.7	1.5	1.5	1.7	1.0	0.4
Total	100.0	100.0	100.0	100.0	100.0	100.0	100.0	100.0	100.0	100.0	100.0	100.0	100.0
DI	33.0	44.6	46.6	51.4	50.8	47.4	56.2	50.6	53.6	53.3	54.8	64.6	36.3
Mg#	59.8	44.8	46.2	44.8	44.9	60.2	61.3	56.1	57.1	52.4	50.5	48.9	77.2
Nb (ppm)	8	14	14	11	9	10	14	10	13	9	11	14	9
Zr	89	163	94	130	105	173	181	176	219	103	197	275	132
Y	26	40	48	23	23	24	23	25	25	24	28	39	24
Sr	1246	1470	1476	1503	1602	1075	679	1200	978	1297	1123	970	286
Rb	78	45	51	66	83	94	137	99	122	83	94	156	94
Ba	2301	1615	1416	3072	2706	2361	1192	2831	2223	2337	2109	1854	990
Ga	22	26	26	25	24	19	22	20	20	21	22	22	17
Zn	180	154	136	122	125	99	80	88	88	90	100	89	84
Cu	30	14	17	8	6	38	32	33	27	27	17	9	9
Ni	90	3	2	3	4	74	116	31	44	19	25	14	345
Co	51	18	16	17	13	34	28	27	25	25	22	18	55
Cr	340	16	12	18	18	254	233	132	151	68	75	42	1321
V	351	146	137	131	122	182	116	190	167	165	172	119	100
Sc	26	19	19	18	19	23	16	22	19	16	17	14	20
La	58.9	80.9	86.7	63.3	52.7	52.6	50.6	51.0	57.6	32.5	53.3	64.0	33.6
Ce	110.0	131.9	117.8	107.5	85.9	84.1	80.6	89.3	100.5	55.6	88.3	101.6	53.0
Pr	14.2	17.8	17.3	13.4	10.9	11.0	9.5	11.2	12.4	6.9	11.1	12.8	7.0
Nd	61.3	75.8	71.7	56.2	46.9	46.7	37.5	46.6	50.8	27.4	46.8	52.4	26.9
Sm	12.1	14.0	15.4	10.2	9.1	9.5	7.3	8.9	9.7	5.9	9.5	10.2	5.8
Eu	2.8	3.4	4.0	3.0	4.0	3.4	2.0	2.3	2.2	2.7	3.2	2.5	1.6
Gd	9.5	11.6	14.1	8.2	8.1	8.3	6.4	7.0	7.5	5.3	8.3	9.9	5.1
Tb	1.1	1.5	1.7	1.0	0.9	1.0	0.8	0.9	0.9	0.7	1.0	1.4	0.7
Dy	5.5	7.8	8.0	5.2	3.9	4.2	3.4	4.4	5.0	3.0	4.4	8.2	3.1
Ho	1.0	1.4	1.4	0.9	0.7	0.8	0.7	0.8	0.9	0.6	0.8	1.6	0.6
Er	2.9	4.1	3.7	2.6	1.8	2.1	1.7	2.3	2.6	1.5	2.2	4.5	1.7
Tm	0.3	0.5	0.5	0.3	0.3	0.3	0.3	0.3	0.3	0.3	0.4	0.6	0.3
Yb	2.0	2.9	3.2	1.9	1.5	1.8	1.6	1.8	2.1	1.4	1.9	3.8	1.6
Lu	0.3	0.4	0.5	0.2	0.3	0.3	0.3	0.2	0.3	0.3	0.3	0.5	0.3
Hf	nm	3.16	nm	nm	nm	3.90	3.20	4.91	5.46	nm	nm	7.18	3.89
Ta	0.42	0.69	0.69	0.60	0.58	0.57	0.92	0.53	0.75	0.49	0.42	0.78	0.48
Pb	9.35	13.63	11.36	15.69	12.29	14.37	22.07	16.57	19.80	14.52	15.63	21.76	10.75
Th	3.29	2.04	2.05	1.86	3.06	4.60	7.38	3.18	6.71	1.48	2.56	11.32	6.59
U	0.65	0.44	0.64	0.40	0.83	1.04	2.31	0.68	1.15	0.56	0.78	2.25	1.35
Zr/Sm	7.34	11.65	6.11	12.71	11.59	18.26	24.92	19.79	22.68	17.57	20.84	27.04	22.90
Th/Ce	0.03	0.02	0.02	0.02	0.04	0.05	0.09	0.04	0.07	0.03	0.03	0.11	0.12
Th/U	5.06	4.61	3.19	4.66	3.67	4.42	3.20	4.70	5.81	2.66	3.27	5.02	4.87
Th/La	0.06	0.03	0.02	0.03	0.06	0.09	0.15	0.06	0.12	0.05	0.05	0.18	0.20
Ce/Pb	11.77	9.68	10.37	6.85	6.99	5.85	3.65	5.39	5.07	3.83	5.65	4.67	4.94
Nb/Ta	19.1	20.2	20.4	18.4	15.6	17.5	15.1	18.9	17.3	18.5	25.9	18.0	18.7
Ba/Nb	287.6	115.4	101.1	279.3	300.7	236.1	85.1	283.1	171.0	259.7	191.7	132.4	110.0
Zr/Nb	11.1	11.6	6.7	11.8	11.7	17.3	12.9	17.6	16.8	11.4	17.9	19.6	14.7
U/La	0.011	0.005	0.007	0.006	0.016	0.020	0.046	0.013	0.020	0.017	0.015	0.035	0.0
K ₂ O/La	0.040	0.023	0.022	0.046	0.052	0.070	0.064	0.079	0.074	0.117	0.072	0.073	0.1

Table 5 (continued)

	Gabbros				Norites								
	NK13	NK10	NK 11	NK 2	NK9	NK 8	GK 0	NK 5	NK7	NK 1	NK 4	NK 3	NK 6
Eu/Eu*	0.78	0.81	0.84	1.00	1.42	1.18	0.89	0.90	0.80	1.50	1.10	0.76	0.89
La _N /Sm _N	3.04	3.63	3.54	3.88	3.65	3.48	4.37	3.59	3.74	3.47	3.53	3.95	3.66
La _N /Yb _N	20.00	18.77	18.60	22.83	23.83	19.73	21.30	19.36	18.75	15.96	18.67	11.59	14.40
Dy _N /Yb _N	1.81	1.73	1.66	1.81	1.69	1.52	1.38	1.59	1.57	1.40	1.47	1.42	1.28

nm = Not measured.

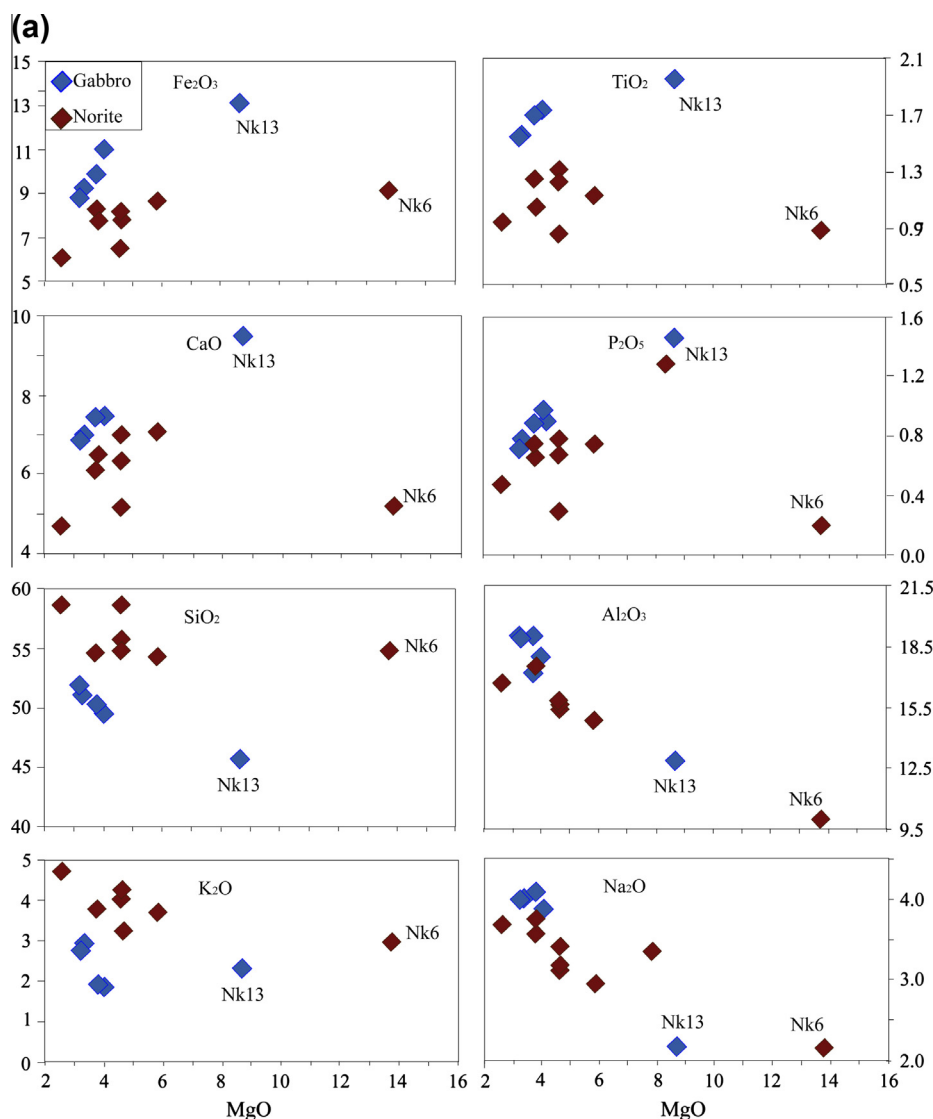


Fig. 7. Harker diagrams of some major element oxides (a) and trace elements (b).

because the late tectonic hydrothermal fluids can be a source of contamination. The large fractures that accompanied emplacement of the pluton can make the fluid circulation easier, and at the same time, can change the dynamical conditions. The instability of large flake of phlogopite associated to orthopyroxene can explain this situation. Indeed, large variations in plagioclase composition, labrador in gabbro, andesine-oligoclase and albite in norites with greenish magnesian phlogopite (alteration to chlorite), is reminiscent of leaching of magmatic mineral. The small pluton like Kekem gabbro-norite which emplaced in richness fluids post-tectonic environment can be transformed easier by endomorphism. This endomorphism can alter gabbro to norite

(Raguin, 1976). Nonetheless, post-magmatic modifications do not seem having affected the Rb–Sr isotopic system (see Section 5.4).

Crustal contamination can be important in the petrogenesis of potassic magmas as they pass through continental crust, especially for plutons. Fractional crystallization associated with crustal contamination (AFC) is an important process during magma evolution (DePaolo, 1981) and may modify both elemental and isotopic compositions. Crustal materials are rich in LILE, K₂O and Na₂O and depleted in P₂O₅ and TiO₂. Therefore, crustal contamination will significantly increase K₂O, Na₂O and LILE. The gabbros and norites exhibit covariation of TiO₂ with MgO, sug-

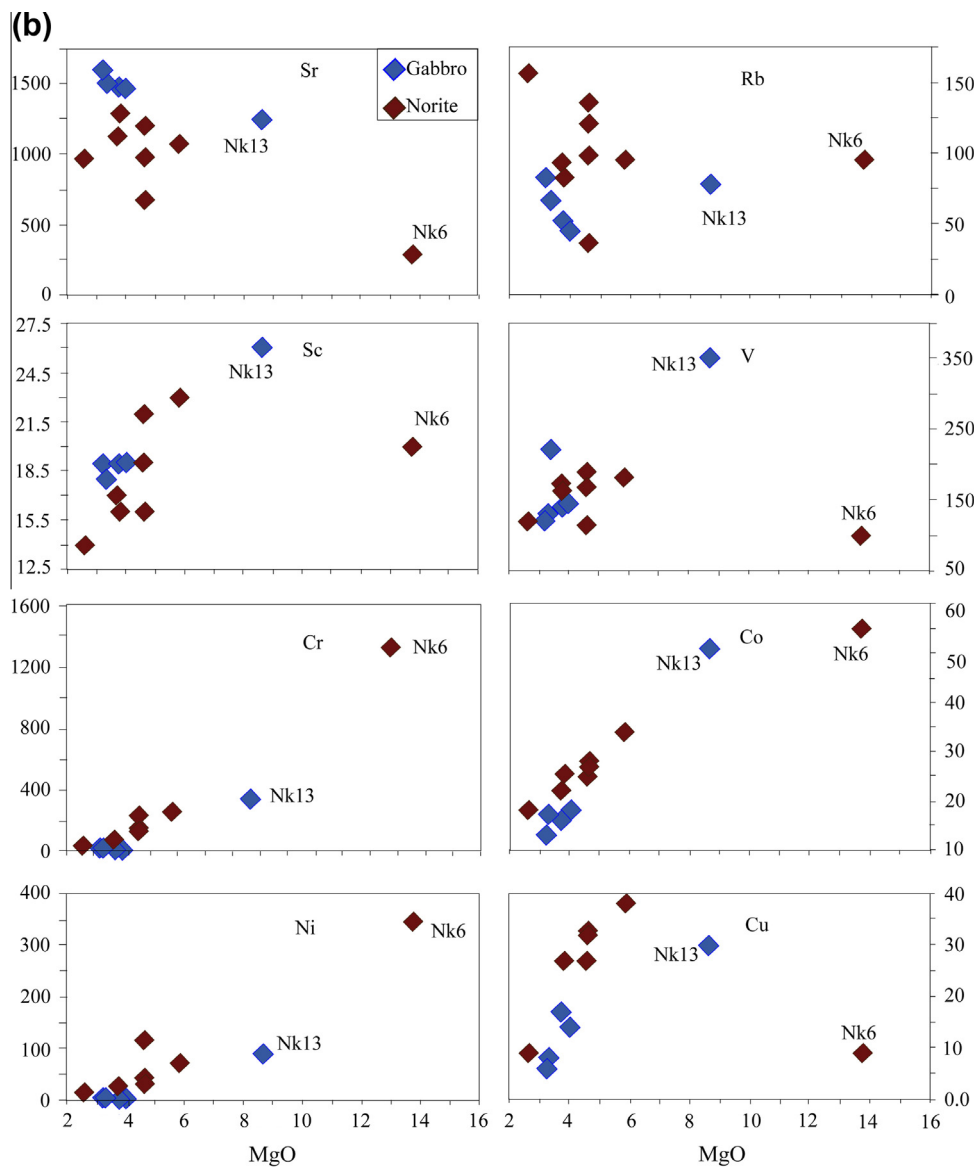


Fig. 7. (continued)

gesting that fractional crystallization was superimposed on crustal contamination. High concentrations of K_2O and constant concentration of Na_2O in both rocks suggest moderate crustal contamination. The Ce/Pb ratios, particularly in norite samples (Fig. 10), confirm this assumption. Higher K_2O and LILE contents in norites could be linked to higher rate of crustal contamination during differentiation but the common Sr and Nd isotopic signature (gabbros are even more radiogenic in Sr isotopes than norites) dismisses this possibility. Indeed, $^{87}Sr/^{86}Sr_{576Ma}$ show negative correlation with $1/Sr * 1000$, SiO_2 , K_2O and MgO in norites (Fig. 10). These are contrary to AFC process as proposed DePaolo (1981). The cause may thus be a slightly more enriched source or a lower degree of partial melting. If a crustal contamination occurred, it was similar for both groups of rocks. In a general way, minor crustal contamination might result in negative Nb–Ta anomalies but also in positive Zr–Hf anomalies due to enrichment of those elements in crustal materials. The studied samples exhibit negative Nb–Ta, negative Zr–Hf anomalies, suggesting that crustal contamination was not important (Green, 2006). The relatively low Zr/Sm ratios (3–25) of those samples

reflect some residual mineral that retains Zr (such as zircon). Such low Zr/Sm ratios cannot result from crustal contamination because the upper crust has generally high Zr/Sm ratios (~32). In addition, the absolute concentrations of incompatible elements (including Nb, Ta, Zr, Sm, etc.) are much higher than those usually observed in crustal rocks (Taylor and McLennan, 1995). Furthermore, the Ba (1192–3072 ppm) and Sr (970–1503 ppm) are much higher than those of the continental crust (Ba = 259 ppm; Sr = 348 ppm; Rudnick and Gao, 2004), implying a strongly enriched source. Whereas, the low Th/Ce ratios (0.02–0.07) and the absence of negative Eu anomalies (except in NK6 (Th/Ce = 0.12), NK3 (Th/Ce = 0.11) and GK0 (Th/Ce = 0.09) also suggest that crustal contamination did not play a significant role in the generation of magmas. Indeed, continental crust has relatively high Th/Ce ratios (~0.15) and negative Eu anomalies (Taylor and McLennan, 1995), while mantle-derived magmas have low Th/Ce ratios (0.02–0.05, Sun and McDonough, 1989).

The enrichment in alkalis, LILE and more generally in incompatible elements must thus be related to the Kekem magma mantle

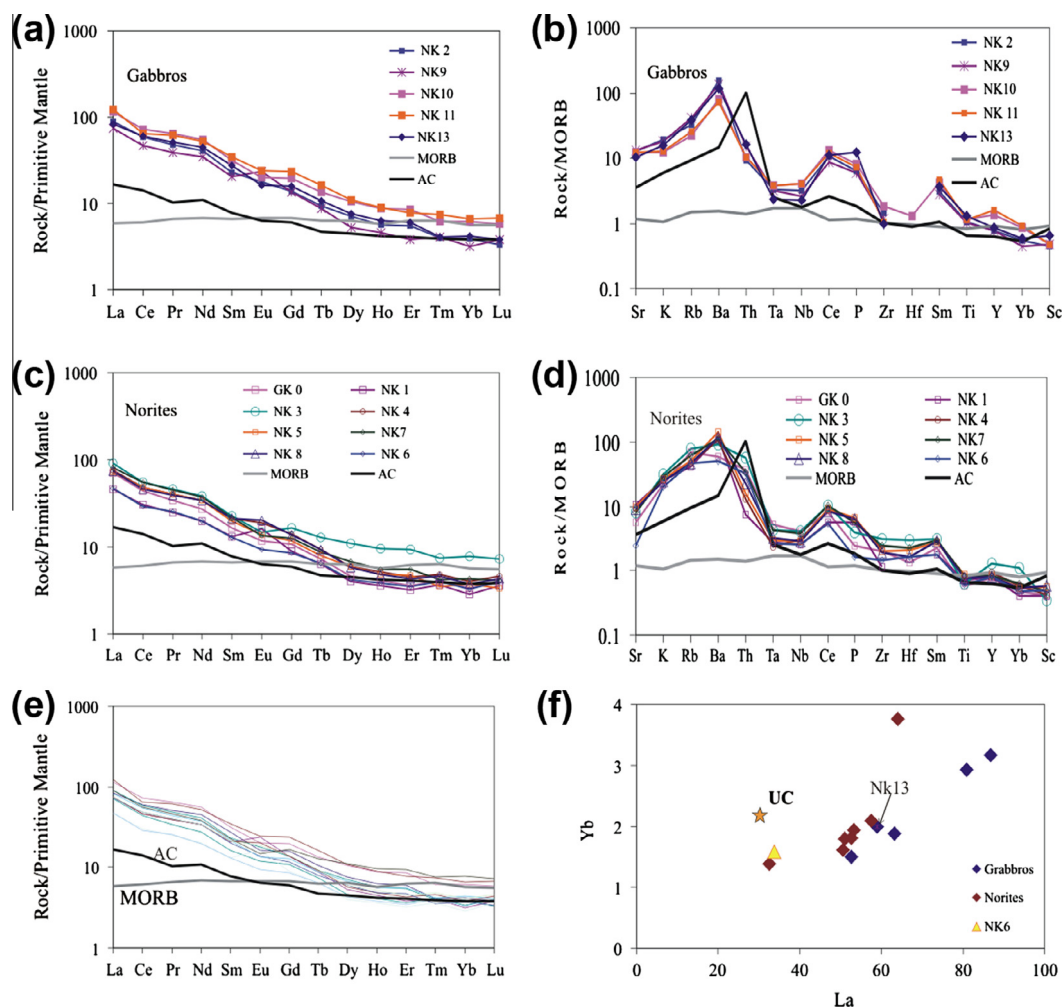


Fig. 8. REE normalised to primitive mantle diagram after McDonough et al. (1992): (a) Gabbros pattern, (b) Spider diagram of gabbro, (c) Norites pattern, (d) Spider diagram of norites, MORB values of normalization are from Pearce (1983), values of average crust (AC) and MORB are from Kelemen et al. (2004) and (e) Gabbros and norites pattern show that their belonging to one source and f attests this assumption.

Table 6
Sr and Nd isotopic data.

	Rb	Sr	⁸⁷ Rb/ ⁸⁶ Sr	⁸⁷ Sr/ ⁸⁶ Sr	2σ	Sr _i 576	Sm	Nd	¹⁴⁷ Sm/ ¹⁴⁴ Nd	¹⁴³ Nd/ ¹⁴⁴ Nd	2σ	εNd ₀	εNd ₅₇₆	T _{DM} (Ga)
<i>Gabbros</i>														
NK9	83	1602	0.1500	0.709481	0.000005	0.708249	9.06	46.85	0.116977	0.511884	0.000004	-14.71	-8.85	1823
NK13	78	1246	0.1812	0.708981	0.000020	0.707493	12.00	63.00	0.115188	0.512021	0.000004	-12.04	-6.04	1577
NK10	45	1470	0.0886	0.708526	0.000010	0.707798	15.76	81.27	0.117271	0.511972	0.000012	-12.99	-7.15	1689
<i>Norites</i>														
NK3	156	970	0.4655	0.710657	0.000009	0.706834	11.56	55.31	0.126395	0.512109	0.000010	-10.32	-5.15	1626
NK4	94	1123	0.2423	0.708910	0.000020	0.706921	9.45	46.83	0.122057	0.512068	0.000004	-11.12	-5.63	1617
NK5	99	1200	0.2388	0.709107	0.000009	0.707146	10.37	50.37	0.124501	0.511994	0.000012	-12.56	-7.26	1788
NK6	94	286	0.9519	0.715818	0.000008	0.708000	5.76	26.94	0.129382	0.511996	0.000003	-12.52	-7.58	1889
NK7	122	978	0.3611	0.710037	0.000009	0.707072	11.05	55.21	0.121034	0.511978	0.000009	-12.87	-7.31	1748
NK8	94	1075	0.2531	0.709175	0.000006	0.707097	9.47	46.72	0.122599	0.512033	0.000003	-11.80	-6.36	1685

source. Geochemical and isotopic data constrains an additional more magnesian and less radiogenic component, as shown by the norite samples (more magnesian and less radiogenic than gabbro samples; Fig. 10). This could be due to the heterogeneity of the lithospheric mantle source or to some input from the Kekem magnesian (Dumort, 1968) garnet sillimanite gneiss surrounding rocks considered to be a northern extension of the Paleoproterozoic Nyong Group (Penaye et al., 2004). This hypothesis is however at variance with the fact that the AFC failed to explain properly the evolution of the Kekem gabbro-norite pluton.

6.2. Constraints on magma source region

The broad geochemical similarities, as shown by the normalised primitive mantle patterns or by the relative homogeneity of Sr and Nd isotopic ratios of the Kekem rocks, suggests a common source for the various facies of the Kekem pluton (Fig. 8f and 10).

The LREE enrichment relatively to HREE ($La_N/Yb_N = 14.2-23.5$) and the flat pattern ($Dy_N/Yb_N = 1.3-1.7$) of the HREE lead to propose firstly a spinel lherzolite peridotite as a mantle source (Mckenzie and O'Nions, 1991). The Th/U (2.7–5.8), Th/La (<0.2)

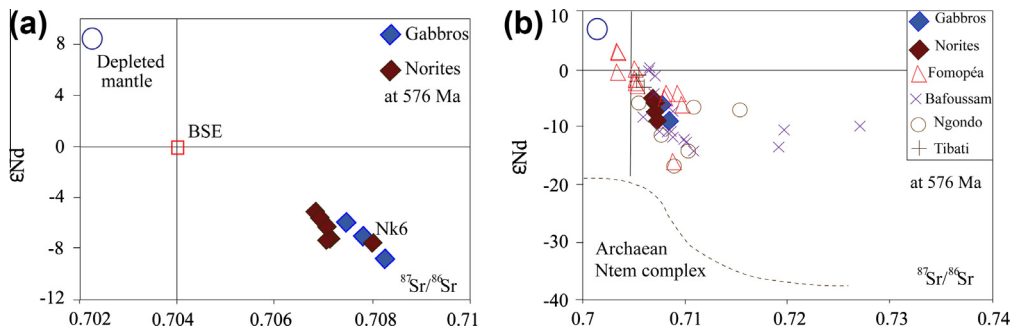


Fig. 9. Sr–Nd isotopic composition of the Kekem complex (a) with representatives of the Archaean Ntem complex (Shang et al., 2004, 2007) and some Palaeoproterozoic high-K granitoids of CCSZ (Ngondo: Tagne-Kamga, 2003, Bafoussam: Djouka-Fonkwé et al., 2008, Tibati, Njanko et al., 2006, Fomopéa: Kwékam et al., 2010) (b); BSE (Bulk Silicate Earth).

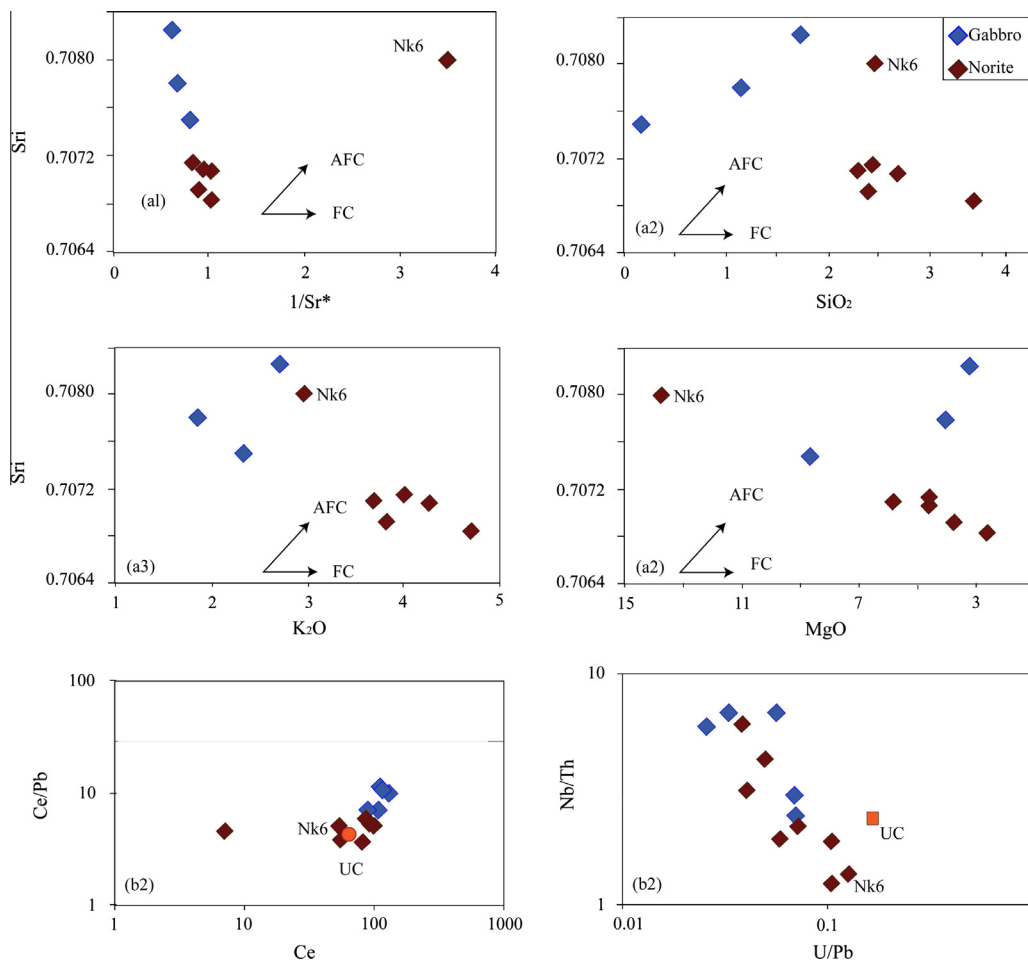


Fig. 10. Plots of Sr_{Ti} ($^{87}Sr/^{86}Sr$)_{576Ma} vs $1/Sr$, Sr_{Ti} vs SiO_2 , Sr_{Ti} vs K_2O , Sr_{Ti} vs MgO show that gabbros and norites are not controlled only by AFC, and Ce/Pb vs Ce and Nb/Th vs U/Pb show that both groups of rocks belong to same source.

and Zr/Nb (11.1–19.6) ratios are close to typical mantle ratios (Taylor and McLennan, 1995; Rudnick et al., 1998).

The budget of the moderately incompatible elements (HREE, HFSE and Ti) is largely controlled by partial melting processes (Pearce and Peate, 1995). In particular, HFSE are used to constrain the nature of the mantle sources which may have been depleted by previous melt extraction in back-arc basins (Elliott et al., 1997) or in arc setting (Grove et al., 2002). Experimental studies reveal that Nb–Ta and Zr–Hf have significantly different partition coefficients in the system Cpx/anhydrous silicate melt (Johnson and Schwab,

2004). In Cpx/melt system, Zr is generally more incompatible than Hf by a factor of 1.5–2, whereas the D_{Nb}/D_{Ta} ratio is less than 1. Therefore, Nb/Ta and Zr/Hf ratios can be significantly fractionated and would be positively correlated during partial melting of the upper mantle. This process would also be expected to yield positive correlations of sub-chondritic Nb/Ta ratios with La/Yb, Th/Yb, Zr/Ti, Ti/V and Y/Sc ratios, which would decrease with increasing depletion of the mantle wedge (Pearce and Peate, 1995). However, the Kekem gabbro–norites do not show such correlations (Fig. 11), suggesting that their mantle source region was a rather primitive

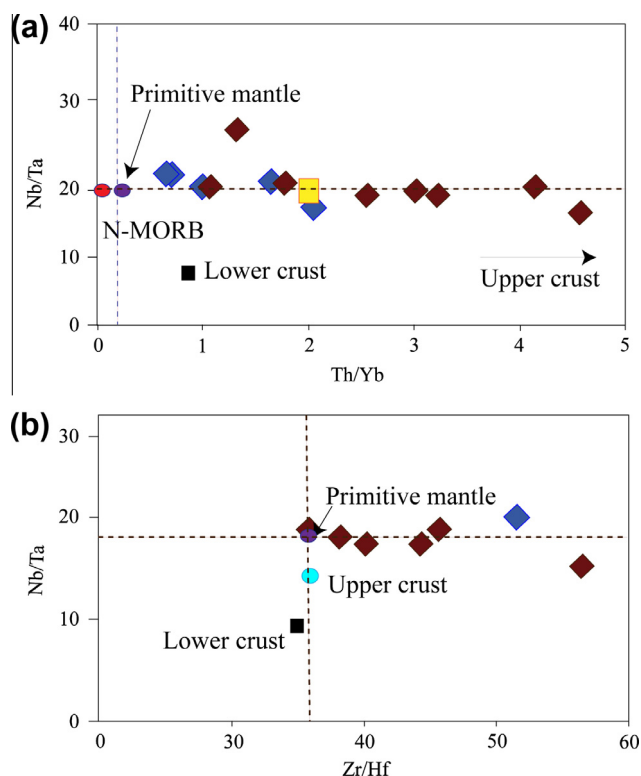


Fig. 11. Plots of Nb/Ta vs Th/Yb (a) and Nb/Ta vs Zr/Hf for the gabbro-norites of Kekem. Values of N-MORB, OIB and primitive mantle are from Sun and McDonough (1989). Values for the upper and lower crust are from Wedepohl (1995). Nb/Ta ratios are constant about 17, value of primitive mantle.

lithospheric mantle, which had not been depleted by previous melt extraction (Pearce and Peate, 1995). The Nb/U (<30) and Nb/Th (<8) ratios of Kekem gabbro-norites are closed to the primitive mantle values. Therefore, the enrichment in LREE suggests a mantle enriched source rather than an evolved magma process implication. Those gabbro-norites have Sm/Yb ratios higher than the spinel-lherzolite melting curve, but lower than the garnet-lherzolite melting trend, such that all of the analyzed samples plot between the two trajectories in side of E-MORB (Fig. 12). In the La/Sm versus Sm/Yb diagram (Fig. 12c), most samples plot between the garnet-spinel-lherzolite (50:50) and spinel < garnet lherzolite curves (about 65–50gt:35–50sp), thus suggesting they derived from a mantle reservoir, slightly deeper than the garnet-spinel lherzolite level. This source region should be located in the spinel-lherzolite and garnet-lherzolite transition zone corresponding to depths of about 70–80 km (Frey et al., 1991; McKenzie et O’Nions, 1991). This could explain the coexistence of two clinopyroxenes in gabbro (high-Al Ti-Cpx and moderately enriched Al Ti-Cpx) that probably implies decreasing of pressure from garnet-lherzolite zone to spinel-lherzolite zone. The rapid decreasing of pressure from gabbro to norite (from 8 kbar to 3 kbar) with low decreasing of temperature could be explained by short transfer time from the magma chamber to the pluton emplacement or rapid exhumation. The rapid exhumation can be one raison of coexistence of two clinopyroxene in gabbro and clinopyroxene-orthopyroxene in norites.

The Kekem gabbro-norites crystallized from melts produced by low partial melting (Fig. 12c). This low degree of partial melting is consistent with their high HFSE contents and high (La/Yb)_N ratios. Relatively high K₂O/La (0.016–0.117) ratios but low U/La (0.004–0.06) ratios in the Kekem gabbro-norites may be also compatible with basaltic magma produced by decompression melting of an already metasomatized mantle source rather than by a flux-driven

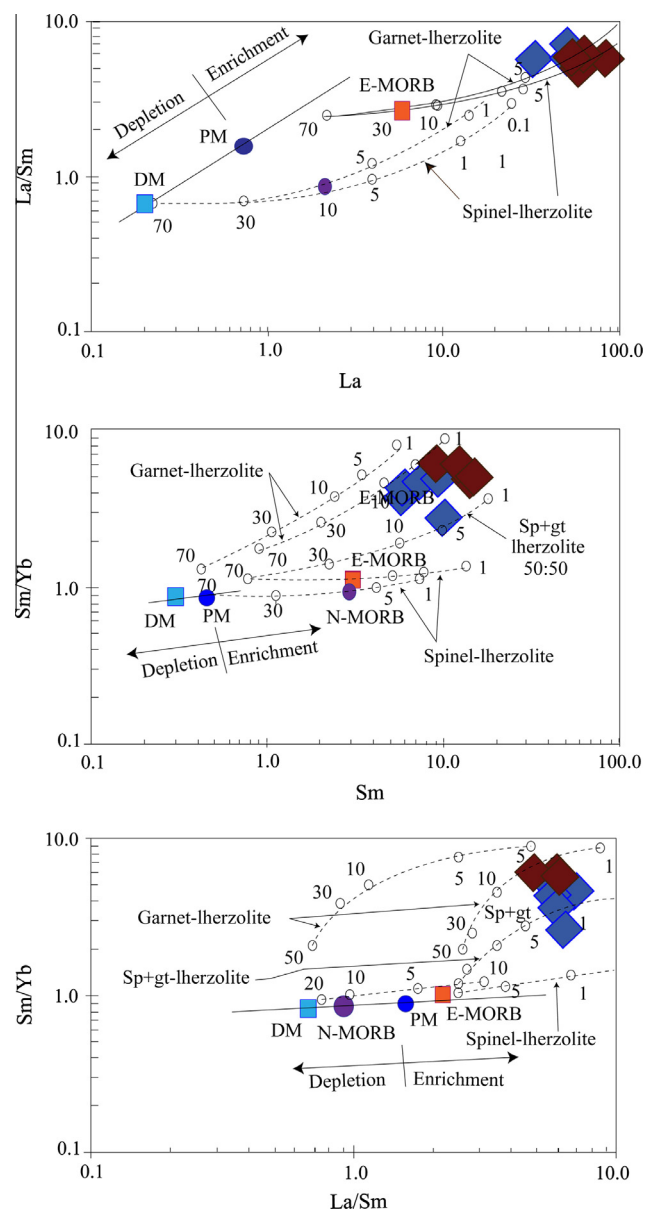


Fig. 12. REE variations in gabbro-norites of Kekem, (a) La vs La/Sm, (b) Sm/Yb vs Sm and (c) Sm/Yb vs La/Sm. Mantle array defined by depleted MORB mantle (DM; McKenzie and O’Nions, 1991) and primitive mantle (PM, Sun and McDonough, 1989) compositions. Melting curves for spinel-lherzolite and garnet-lherzolite sources with both DM and PM compositions after Aldanmaz et al. (2000); circled dots on each melting curve correspond to degrees of partial melting for a given mantle source. Also shown are N-MORB and E-MORB compositions of Sun and McDonough (1989).

melting process (Hochstaedter et al., 1996) (see Section 6.3 for explanation).

This is in agreement with Sr and Nd isotope constraints that imply an old source enriched in LREE and in LILE (Rb) for allowing the acquisition of an enriched isotopic composition (high ⁸⁷Sr/⁸⁶Sr and low ε_{Nd}). This lead to the conclusion that the source of the Kekem rocks is an already metasomatized mantle. Nd–Sr isotopes indicate that this earlier enrichment occurred at least 1 Gyr before the Kekem intrusion. NdT_{DM} model ages correspond to the mean age of the source of the magma (see Liégeois and Stern, 2010 for a detailed discussion of T_{DM} model ages). Their value (1.6–1.9 Ga) imply the major participation of a Paleoproterozoic lithosphere with a limited participation of the Neoproterozoic asthenosphere, playing the role of heat supply. This major Paleoproterozoic lithospher-

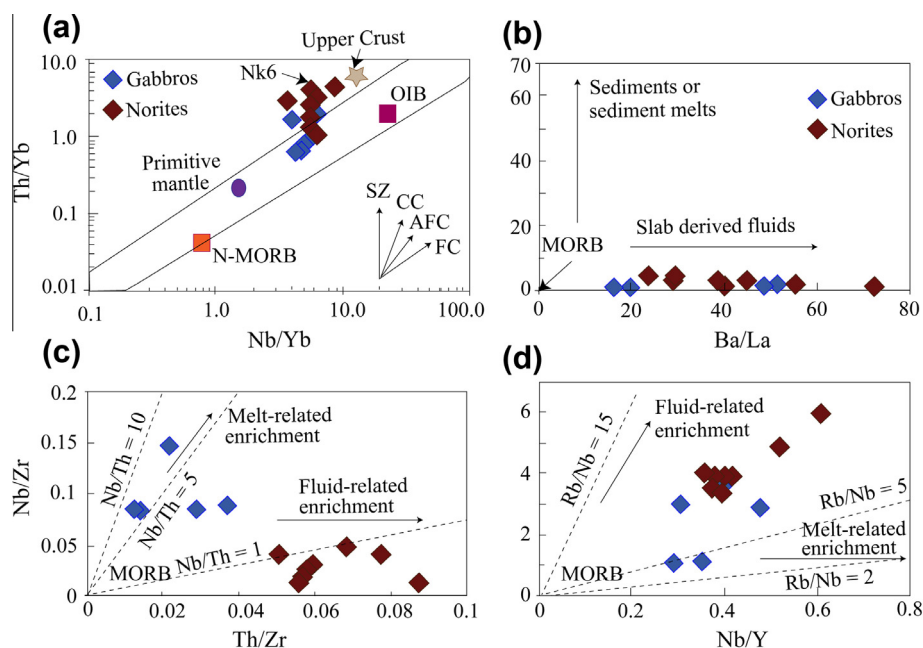


Fig. 13. (a) Nb/Yb vs. Th/Yb diagram shows the importance of subduction environment in the generation of gabbro-norite magma (SZ, subduction zone, CC, continental crust, AFC, assimilation fractional crystallisation, FC, fractional crystallisation), (b) Ba/La vs. Th/Yb, (c) Nb vs. Th/Zr and (d) Rb/Y vs. Nb/Y diagrams after (Green, 2006), show the influence of slab derived fluids during the generation of the gabbro-norite magma.

ic source corresponds to the lithospheric mantle of the Congo craton.

6.3. Source of enrichment

It has been shown that the enrichment in LILE and LREE in the Kekem gabbro-norites resulted from an enrichment from an old lithospheric source and not from a crustal contamination during ascent. REE generally played a significant role in characterizing and identifying the processes that create incompatible element enrichment in mantle rock. Dawson (1984) defined two end products of mantle enrichment processes as patent and cryptic metasomatism. Patent metasomatism, also known as modal metasomatism, is characterized by LREE enrichment accompanied by the presence of hydrous minerals whereas cryptic metasomatism is characterized by a similar style of compositional enrichment without the presence of hydrous minerals. The abundance of apatite and hydrous minerals (such as phlogopite) in the studied rocks can be linked to their large amounts of incompatible elements and fluids. The presence of phlogopite and apatite suggests source enrichment in these incompatible and volatile elements by metasomatism (Bonin, 2004). Furthermore, the low Nb/U ratios (5–20) of the Kekem gabbro-norites also suggest metasomatized lithospheric mantle (Plank, 2005). The presence of negative Nb, Ta, Hf, Zr and Ti anomalies in the MORB-normalised trace element patterns (Fig. 8b–d) could be linked to subduction related magmas (Fig. 13a). Moreover the high Ba/Nb ratios (85–301) lead to propose a subduction-related environment for the enrichment of the source of the Kekem rocks. Indeed, the subduction geodynamic model is recently proposed for the central African pan-African fold belt by Ngako and Njonfang (2011). Some information can be obtained about the source of these elements. Enrichment in Rb, Ba, K (Fig. 8b–d), high K/Nb, La/Nb and low Ce/Pb ratios are consistent with slab-derived enrichment fluids. Whereas, relative to mid-ocean ridge basalt, subducting sediments are strongly enriched in a number of elements of interest, including K, Rb, Sc, Ba, Sr, U, Th, Pb, Sm, Nd, Lu, and Hf are moderately enriched (Morris and Ryan, 2004). The low Ce/Pb ratios (3.8–11.8) of the Kekem rocks

are distinct from those of oceanic basalts (Hofmann et al., 1986), which have high Ce/Pb (~25) ratios (Ben Othman et al., 1989). The low Ce/Pb ratios of the Kekem rocks are due to Pb-enrichment. Experimental data suggest that Ce/Pb ratios of the slab-derived fluids could be as low as ~0.1 or even lower (Brenan et al., 1995; Keppeler, 1996; Ayers, 1998). The relatively low Ce/Pb ratios of the Kekem rocks suggest contribution of slab-derived fluids rather than from subducted sediments or from melts resulting from these sediments (Fig. 13). In addition, the Kekem gabbro-norites have relatively high Rb/Y and low Nb/Zr ratios (Fig. 13c and d), features that resemble magmas produced by interaction between slab-derived fluids and sub-arc mantle peridotites (Green, 2006). Gabbros display higher Nb/Zr ratio than norites; this would indicate that the gabbros are more melt-related enriched than norites that would be more enriched in fluids. This suggests that enrichment in Th may be due to the fluids. Indeed, in the Nb/Yb vs. Th/Yb diagram, gabbros are mostly close to the mantle array while norites evolve along subduction trend.

In summary, geochemical data indicate that the primary magma of the Kekem gabbro-norite pluton was derived from the partial melting of a metasomatized lithospheric mantle (as garnet + spinel lherzolite peridotite), whose metasomatism occurred through slab-derived hydrous fluids generated during a previous subduction process.

Sr–Nd isotopes bring the additional information that this earlier subduction process occurred at least 1 Gyr before the intrusion of the Kekem pluton, during the Palaeoproterozoic or the Archaean, following the asthenospheric material proportion involved in the melting of the Kekem magma. The trends observed in the ϵ_{Nd} vs. $(^{87}Sr/^{86}Sr)_i$ at 576 Ma diagram (Figs. 9 and 10) and the local geology, that displays Palaeoproterozoic relic Nyong series extension (Penaye et al., 2004), would rather favour a Palaeoproterozoic subduction period. If a mantle is modified during a subduction event and does not convect afterwards into a hot part of the mantle wedge, the subduction signature could remain indefinitely and remains available to be tapped by upper mantle melting in other tectonic settings (Liégeois et al., 1998; Morris and Ryan, 2004).

6.4. Geodynamical implications

The habitus of the Kekem pluton and its age (576 ± 4 Ma) indicate that it is a post-collisional event. Metasomatized lithospheric mantle is known to be melted during the post-collisional period (Liégeois et al., 1998). The partial melting of a mantle previously enriched in LILE (especially K) induces a second enrichment in these incompatible elements, leading to a K-rich magmatism (Roberts and Clemens, 1993; Liégeois et al., 1998), which is the case of the Kekem pluton.

The Kekem pluton is associated to others K-rich post-collisional plutons in the mixing line between primitive mantle magma and lower crust melt (Fig. 9b). All these plutons are located along the CCSZ (see Fig. 1b for their emplacement). The genesis of these others plutons can be linked to the successive melting of the sources initiated by the rising isotherms during a syn- to post-collisional setting which followed a subduction (Tagne-Kamga, 2003; Njanko et al., 2006; Djouka-Fonkwé et al., 2008; Kwékam et al., 2010; Ngako and Njonfang, 2011). Regionally, the Kekem complex intruded during the D4 tectonic event that occurred in a transpressive environment, evolving towards a transtensional environment. This tectonic event is mainly materialised along the Central Cameroon shear zone (CCSZ, Toteu et al., 2004; Ngako et al., 2008). In an intra-continental setting, such movements along lithospheric-scale shear zones are prone to induce lithospheric delamination, resulting in asthenosphere uprise leading to partial melting of the lithospheric mantle and even crust (Liégeois et al., 2003; Shang et al., 2010; Fezaa et al., 2010). Low crustal contamination of Kekem gabbro-norites massif and alkali-calcic affinity are additional arguments that support a lithosphere delamination model (Bonin, 2004). During a collision/post-collision event, this is particularly true when the lower plate (former passive margin) is considered: it is too cold and rigid to be completely remobilized but is submitted to sufficiently intense stress to be tectonically dissected and invaded by magmas, which correspond to a metacratonization process (Ennih and Liégeois, 2008). This was the case of the studied area that corresponds to the northern edge of the Congo craton incorporated within the Pan-African orogen through continental subduction (marked by the Yaoundé nappe thrusting), leading to its metacratonization (Kwékam et al., 2010; Shang et al., 2010). The Kekem complex represents one of the last events of this partial reactivation of a craton boundary, here including the low degree partial melting of its lithospheric mantle.

Tomographic data show that the Kekem complex (576 ± 4 Ma), as the older Fomopéa pluton (622 ± 4 Ma), is located along the northern boundary of the thick lithosphere of the Congo craton (Kwékam et al., 2010). This reveals that the CCSZ marks the lithospheric boundary of the Congo craton, along which the Cameroon volcanic Line also has occurred during the Cenozoic.

7. Conclusions

The Kekem shoshonitic gabbro-norite complex is dated here at 576 ± 4 Ma, which points to a post-collisional emplacement for the HKCA magmatism in the central or Adamawa-yadé domain of the Pan-African fold belt in Cameroon. Major elements and REE indicate that the source of the gabbro-noritic magma of Kekem was located close to the base of the garnet-spinel lherzolite peridotite mantle at 70–80 km depth, within the lithospheric mantle. This lithospheric mantle was metasomatized during an earlier subduction event that probably occurred during the Palaeoproterozoic. The partial melting of this mantle source is related to large movements along the Central Cameroon shear zone (CCSZ) which was active during the period 620–540 Ma. Those movements led to the metacratonization of the northern boundary of the Congo cra-

ton (Kwékam et al., 2010). The Palaeoproterozoic and maybe Archaean inherited mantle component in the post-collisional Kekem gabbro-noritic magma confirms that the CCSZ corresponds to the northern lithospheric boundary of the Congo craton.

Acknowledgments

This study was performed during a postgraduate fellowship of the first author at “CEREGE-Aix-Marseille Université”, financed by SCAC (Service de la Coopération et d'Action Culturelle) of French Republic, and his stay in “Geowissenschaftliches Zentrum Göttingen, Universität Göttingen”, financed by the Germany Academic Exchange Organisation (DAAD). MK is grateful to Gerhard Wörner of “Universität Göttingen” for his supervision. The constructive comments by two anonymous reviewers are gratefully acknowledged; they contributed to a significant amelioration of this paper.

References

- Abdelsalam, M.G., Liégeois, J.P., Stern, R.J., 2002. The Saharan metacraton. *Journal of African Earth Sciences* 34, 119–136.
- Aldanmaz, E., Pearce, J.A., Thirlwall, M.F., Mitchell, J.G., 2000. Petrogenetic evolution of the late Cenozoic, post-collision volcanism in western Anatolia, Turkey. *Journal of Volcanology and Geothermal Research* 102, 67–95.
- Ayers, J., 1998. Trace element modelling of aqueous fluid-peridotite interaction in the mantle wedge of subduction zones. *Contribution to Mineralogy and Petrology* 132, 390–404.
- Ben Othman, D., White, W.M., Patchett, J., 1989. The geochemistry of marine sediments, island arc magma genesis, and crust-mantle recycling. *Earth Planetary Science Letter* 94, 1–21.
- Bonin, B., 2004. Do coeval mafic and felsic magmas in post-collisional to within-plate regimes necessarily imply two contrasting, mantle and crustal, sources? A review *Lithos* 78, 1–24.
- Bosch, D., Bruguier, O., Pidgeon, R.T., 1996. The evolution of an Archaean metamorphic belt: A conventional and SHRIMP U–Pb study of accessory minerals from the Jimperding metamorphic belt, Yilgarn craton, Western Australia. *Journal of Geology* 104, 695–711.
- Bosch, D., Garrido, C.J., Bruguier, O., Dhuime, B., Bodinier, J.L., Padrón-Navarta, J.A., Galland, B., 2011. Building an island-arc crustal section: time constraints from a LA-ICP-MS zircon study. *Earth and Planetary Science Letters* 309, 268–279.
- Brenan, J.M., Shaw, H.F., Ryerson, F.J., 1995. Experimental evidence for the origin of lead enrichment in convergent-margin magmas. *Nature* 378, 54–56.
- Bruguier, O., Hammor, D., Bosch, D., Caby, R., 2009. Miocene incorporation of peridotite into the Hercynian basement of the Maghrebides (Edough massif, NE Algeria): implications for the geodynamic evolution of the Western Mediterranean. *Chemical Geology* 261, 171–183.
- Castaing, C., Feybesse, J.L., Thiebaut, D., Triboulet, C., Chevremont, P., 1994. Palaeogeographical reconstructions of the Pan-African/Brasiliano Orogen; closure of an oceanic domain or intracontinental convergence between major blocks? *Precambrian Research* 69, 327–344.
- Dawson, J.B., 1984. Contrasting types of upper-mantle metasomatism? In: Kornprobst, J. (Ed.), *Kimberlites II: The Mantle and Crust-mantle Relationships*. Elsevier, Amsterdam, pp. 289–294.
- DePaolo, D.J., 1981. Trace element and isotopic effects of combined wallrock assimilation and fractional crystallization. *Earth Planetary Science Letters* 53, 189–202.
- Djouka-Fonkwé, M.L., Schulz, B., Schüssler, U., Tchouankoué, J.P., Nzolang, C., 2008. Geochemistry of the Bafoussam Pan-African I- and S-type granitoids in western Cameroon. *Journal of African Earth Sciences* 50, 148–167.
- Dumort, J.-C., 1968. Carte géologique de reconnaissance à l'échelle du 1/50000^{ième}, République Fédérale du Cameroun, Notice explicative sur la feuille Douala-Ouest. Direction des Mines et de la Géologie du Cameroun.
- Elliott, T., Plank, T., Zindler, A., White, W., Bourdon, B., 1997. Element transport from slab to volcanics and front at the Mariana arc. *Journal Geophysical Research* 102, 14991–15019.
- Ennih, N., Liégeois, J.P., 2008. The boundaries of the West African craton, with a special reference to the basement of the Moroccan metacratonic Anti-Atlas belt. In: Ennih, N., Liégeois, J.-P. (Eds.), *The Boundaries of the West African Craton*. Geological Society, London, Special Publications, vol. 297, pp. 1–17.
- Fezaa, N., Liégeois, J.P., Abdallah, N., Cherfouh, E.H., De Waele, B., Bruguier, O., Ouabadi, A., 2010. Late ediacaran geological evolution (575–555 Ma) of the Djanet Terrane, Eastern Hoggar, Algeria, evidence for a Murzukian intracontinental episode. *Precambrian Research* 180, 299–327.
- Frey, F.A., Garcia, M.O., Wise, W.S., Kennedy, A., Gurrier, P., Albarede, F., 1991. The evolution of Mauna Kea volcano, Hawaii: petrogenesis of tholeiitic and alkalic basalts. *Journal Geophysical Research* 96, 14347–14375.
- Frost, B.R., Barnes, C.G., Collins, W.J., Arculus, R.J., Ellis, D.J., Frost, C.D., 2001. A geochemical classification for granitic rocks. *Journal of Petrology* 42, 2033–2048.

- Fuhrman, M.L., Lindsley, D.H., 1998. Ternary-feldspar modeling and thermometry. *American Mineralogist* 73, 201–215.
- Green, N.L., 2006. Influence of slab thermal structure on basalt source regions and melting conditions: REE and HFSE constraints from the Garibaldi volcanic belt, northern Cascadia subduction system. *Lithos* 87, 23–49.
- Grove, T.L., Parman, S.W., Bowring, S.A., Price, R.C., Baker, M.B., 2002. The role of an H₂O-rich fluid component in the generation of primitive basaltic andesites and andesites from the Mt Shasta region, N. California. *Contributions Mineralogy Petrology* 142, 375–396.
- Hofmann, A.W., Jochum, K.P., Seufert, M., White, W.M., 1986. Nb and Pb in oceanic basalts: new constraints on mantle evolution. *Earth Planetary Science Letter* 79, 33–45.
- Horstwood, M.S.A., Foster, G.L., Parrish, R.R., Noble, S.R., Nowell, G.R., 2003. Common-Pb corrected in situ U–Pb accessory mineral geochronology by LA-MC-ICP MS. *Journal of Analytical Atomic Spectroscopy* 18, 837–846.
- Johnson, A.D., Schwab, B.E., 2004. Constraints on clinopyroxene/melt partitioning of REE, Sr, Ti, Cr, Zr, and Nb during mantle melting: first insights from direct lherzolite melting experiments at 1.0 GPa. *Geochimica et Cosmochimica Acta* 68, 4949–4962.
- Kelemen, P.B., Høghøj, K., Greene, A.R., 2004. One view of the geochemistry of subduction-related magmatic arcs, with an emphasis on primitive andesite and lower crust. In: *Treatise on geochemistry. The Crust*, editor Rudnick, vol. 3, pp. 593–659.
- Keppler, H., 1996. Constraints from partitioning experiments on the compositions of subduction-zone fluids. *Nature* 380, 237–240.
- Kwékam, M., 2005. Genèse et évolution des granitoïdes calco-alcalins au cours de la tectonique panafricaine: le cas des massifs syn à tardi-tectonique de l'Ouest-Cameroun (régions de Dschang et de Kekem). Thèse Doct. Etat Univ., Yaoundé I, 194 p.
- Kwékam, M., Njonfang, E., Tchoua, F., 2007. The post-collisional norites of Kekem, West-Cameroon part of the Pan-African fold belt: possible relation between Pan-African subduction zone and their magma. 5ème Colloque international 3MA Fez- Morocco. Abstracts, 10–12 May, 2007, pp. 143–144.
- Kwékam, M., Liégeois, J.P., Njonfang, E., Affaton, P., Hartmann, G., Tchoua, F., 2010. Nature, origin and significance of the Fomopéa Pan-African high-K calc-alkaline plutonic complex in the Central African fold belt (Cameroon). *Journal African Sciences* 54, 79–95.
- Liégeois, J.-P., Stern, R.J., 2010. Sr–Nd isotopes and geochemistry of granite-gneiss complexes from the Meatiq and Hafafit domes, Eastern Desert, Egypt: No evidence for pre-Neoproterozoic crust. *Journal of African Earth Sciences* 57, 31–40.
- Liégeois, J.-P., Navez, J., Hertogen, J., Black, R., 1998. Contrasting origin of post-collisional high-K calc-alkaline and shoshonitic versus alkaline and peralkaline granitoids. The use of sliding normalization. *Lithos* 45, 1–28.
- Liégeois, J.-P., Latouche, L., Boughara, M., Navez, J., Guiraud, M., 2003. The LATEA metacraton (Central Hoggar, Tuareg shield, Algeria): behaviour of an old passive margin during the Pan-African orogeny. *Journal African Earth Sciences* 37, 161–190.
- Ludwig, K.R., 2000. Decay constant errors in U–Pb Concordia intercept ages. *Chemical Geology* 166, 315–318.
- McDonough, W.F., Sun, S.S., Ringwood, A.E., Jagoutz, E., Hofmann, A.W., 1992. Potassium, rubidium, and cesium in the Earth and Moon and the evolution of the mantle of the Earth. *Geochimical Cosmochimical Acta* 56, 1001–1012.
- McKenzie, D., O'Nions, R.K., 1991. Partial melt distribution from inversion of rare earth element concentrations. *Journal of Petrology* 32, 1021–1091.
- Merlet, C., 1994. An accurate computer correction program for quantitative electron probe microanalysis. *Mikrochimica Acta* 114 (115), 363–376.
- Morimoto, N., Fabries, J., Ferguson, A.K., Ginzburg, I.V., Ross, M., Seifert, F.A., Zussman, J., Aoki, K., Gottardi, G., 1988. Nomenclature of pyroxenes. *American Mineralogist* 73, 1123–1133.
- Morris, J.D., Ryan, J.G., 2004. Subduction zone processes and implications for changing composition of the upper and lower mantle. In: Carlson, R.W. (Ed.), *The Mantle and Core, Treatise on Geochemistry* 2, Holland, H.D. and Turekian, K.K., Executive Editors, pp. 451–470.
- Ngako, V., 1999. Les déformations continentales panafricaines en Afrique centrale. Résultat d'un poinçonnement de type himalayen. Thèse Doct. Etat Univ. Yaoundé I, p. 301.
- Ngako, V., Njonfang, E., 2011. Plates amalgamation and plate destruction, the Western Gondwana history. In *Plate in Damien Closson Intech eds*, pp. 1–36.
- Ngako, V., Affaton, P., Nnanga, J.M., Njanko, Th., 2003. Pan-African tectonic evolution in central and southern Cameroon: transpression and transtension during sinistral shear movements. *Journal of African Earth Sciences* 36, 207–214.
- Ngako, V., Affaton, P., Njonfang, E., 2008. Pan-African tectonics in northwestern Cameroon: implication for the history of western Gondwana. *Gondwana Research* 14, 509–522.
- Njanko, T., Nédélec, A., Affaton, P., 2006. Synkematic high-k calc-alkaline plutons associated with the Pan-African Central Cameroon shear zone (W-Tibati area): petrology and geodynamic significance. *Journal of African Earth Sciences* 44 (4–5), 494–501.
- Njanko, T., Nédélec, A., Kwékam, M., Siqueira, R., Esteban, L., 2010. Emplacement and deformation of the Fomopéa pluton: implication for the Panafrican history of Western Cameroon. *Journal of Structural Geology* 32, 306–320.
- Njonfang, E., Ngako, V., Kwékam, M., Affaton, P., 2006. Les orthogneiss calco-alcalins de Fouban-Bankim: témoins d'une zone interne de marge active panafricaine en cisaillement. *Comptes Rendus Geoscience* 338, 606–616.
- Pearce, J.A., 1983. Role of the sub-continental lithosphere in magma genesis at active continental margins. In: Hawkesworth, C.J., Norry, M.J. (Eds.), *Continental Basalts and Mantle Xenoliths*. Shiva, Nantwich, pp. 230–249.
- Pearce, J.A., Peate, D.W., 1995. Tectonic implications of the composition of volcanic arc magmas. *Annual Review Earth Planetary Sciences* 23, 252–285.
- Peccherillo, A., Taylor, S.R., 1976. Geochemistry of Eocene calc-alkaline volcanic rocks from the Kastamonu area, Northern Turkey. *Contributions to Mineralogy and Petrology* 58, 63–81.
- Pedersen, R.B., Dunning, G.R., 1997. Evolution of arc crust and relations between contrasting sources: U–Pb (age) Nd and Sr isotope systematics of the ophiolitic terrain of SW Norway. *Contributions to Mineralogy and Petrology* 128, 1–15.
- Penaye, J., Toteu, S.F., Tchameni, R., Van Schmus, W.R., Tchakounté, J., Ganwa, A., Minyem, D., Nsifa, E.N., 2004. The 2.1 Ga West Central African belt in Cameroon: extension and evolution. *Journal of African Earth Sciences* 39, 159–164.
- Plank, T., 2005. Constraints from Thorium/Lanthanum on sediment recycling at subduction zones and the evolution of the continents. *Journal of Petrology* 46, 921–944.
- Putirka, K., 2008. Thermometers and barometers for volcanic systems. *Reviews in Mineralogy and Geochemistry* 69, 61–120.
- Raguin, E., 1976. *Géologie du granite*, 3rd ed. Masson Paris, 274p.
- Roberts, M.P., Clemens, J.D., 1993. Origin of high-potassic, calc-alkaline, I-type granitoids. *Geology* 21, 825–828.
- Rudnick, R.L., McDonough, W.F., O'Connell, R.J., 1998. Thermal structure, thickness and composition of continental lithosphere. *Chemical Geology* 145, 395–411.
- Schärer, U., Krogh, T.E., Gower, C.F., 1986. Age and evolution of the Grenville Province in eastern Labrador from U–Pb systematics in accessory minerals. *Contributions to Mineralogy and Petrology* 94, 438–451.
- Shang, C.K., Satir, M., Siebel, W., Nsifa, E.N., Taubald, H., Liégeois, J.P., Tchoua, F.M., 2004. TTG magmatism in the Congo craton; a view from major and trace element geochemistry, Rb–Sr and Sm–Nd systematics: case of the Sangmelima region, Ntem complex, southern Cameroon. *Journal of African Earth Sciences* 40, 61–79.
- Shang, C.K., Satir, M., Nsifa, E.N., Liégeois, J.P., Siebel, W., Taubald, H., 2007. Archaean high-K granitoids produced by remelting of earlier Tonalite-Trondhjemite-Granodiorite (TTG) in the Sangmelima region of the Ntem Complex of the Congo craton, southern Cameroon. *International Journal Earth Sciences* 96, 817–841.
- Shang, C.K., Liégeois, J.P., Satir, M., Frisch, W., Nsifa, E.N., 2010. Late Archaean high-K granite geochronology of the northern metacratonic margin of the Archaean Congo craton, southern Cameroon: evidence for Pb-loss due to non-metamorphic causes. *Gondwana Research* 18, 337–355.
- Steiger, N.J., Jäger, E., 1977. Subcommission on geochronology: convention in the use of decay constants in geo- and cosmochronology. *Earth and Planetary Science Letter* 36, 359–362.
- Sun, S.-S., McDonough, W.F., 1989. Chemical and isotopic systematics of oceanic basalts: implications for mantle composition and processes. In: Saunders, A.D., Norry, M.J. (Eds.), *Magmatism in the Ocean Basins*. Geological Society, Oxford, pp. 313–345.
- Tagne-Kamba, G., 2003. Petrogenesis of the Neoproterozoic Ngondo plutonic complex West Cameroon (Central Africa): a case of late-collision ferro-potassic magmatism. *Journal of African Earth Sciences* 36, 149–171.
- Taylor, S.R., McLennan, S., 1995. The geochemical composition of the continental crust. *Review of Geophysics* 33, 241–265.
- Toteu, S.F., Van Schmus, W.R., Penaye, J., Michard, A., 2001. New U–Pb and Sm–Nd data from north-central Cameroon and its bearing on the pre-Pan African history of central Africa. *Precambrian Research* 108, 45–73.
- Toteu, S.F., Penaye, J., Poudjoun Djomani, Y.H., 2004. Geodynamic evolution of the Pan-African belt in Central Africa with special reference to Cameroon. *Canada Journal Earth Science* 41, 73–85.
- Toteu, S.F., Yongue Fouateu, R., Penaye, J., Tchakounte, J., Seme Mouangue, A.C., Van Schmus, E., Deloule, W.R., Stendal, H., 2006. U–Pb dating of plutonic rocks involved in the nappe tectonic in southern Cameroon: consequence for the Pan-African orogenic evolution of the central African fold belt. *Journal of African Earth Sciences* 44, 479–493.
- Wedepohl, K.H., 1995. The composition of the continental crust. *Geochimica et Cosmochimica Acta* 59, 1217–1232.
- Wiedenbeck, M., Allé, P., Corfu, F., Griffin, W.L., Meier, M., Oberli, F., VonQuadt, A., Roddick, J.C., Spiegel, W., 1995. Three natural zircon standards for U–Th–Pb, Lu–Hf, trace element and REE analysis. *Geostandards Newsletter* 19, 1–23.